



HAL
open science

Optimizing TRISHNA TIR channels configuration for improved land surface temperature and emissivity measurements

Thomas H G Vidal, Philippe Gamet, Albert Olios, Frédéric Jacob

► To cite this version:

Thomas H G Vidal, Philippe Gamet, Albert Olios, Frédéric Jacob. Optimizing TRISHNA TIR channels configuration for improved land surface temperature and emissivity measurements. Remote Sensing of Environment, 2022, 272, pp.112939. 10.1016/j.rse.2022.112939 . hal-03577600

HAL Id: hal-03577600

<https://hal.science/hal-03577600>

Submitted on 16 Feb 2022

HAL is a multi-disciplinary open access archive for the deposit and dissemination of scientific research documents, whether they are published or not. The documents may come from teaching and research institutions in France or abroad, or from public or private research centers.

L'archive ouverte pluridisciplinaire **HAL**, est destinée au dépôt et à la diffusion de documents scientifiques de niveau recherche, publiés ou non, émanant des établissements d'enseignement et de recherche français ou étrangers, des laboratoires publics ou privés.

Optimizing TRISHNA TIR channels configuration for improved land surface temperature and emissivity measurements

Thomas H. G. Vidal^{a,*}, Philippe Gamet^b, Albert Olios^c, Frederic Jacob^d

^a*ACRI-ST, Toulouse, France*

^b*CNES, Toulouse, France*

^c*UMR EMMAH, INRAE, Avignon University, 84000 Avignon, France*

^d*UMR LISAH, University of Montpellier, IRD, INRAE, Institut Agro - Montpellier SupAgro, Montpellier, France*

Abstract

In preparation of the Thermal infraRed Imaging Satellite for High-resolution Natural resource Assessment (TRISHNA) mission, we conducted a thorough analysis of sensitivity for the Temperature-Emissivity Separation (TES) method to the position of the four TRISHNA spectral channels, notably to find an optimal spectral configuration. To that purpose, we designed a fast-computing end-to-end simulator including several components, which we implemented to simulate both pixel-size TRISHNA measurements and land surface temperature (LST) retrievals. Firstly, simulations were conducted over a wide range of realistic scenarii, notably by including vegetation canopy-scale cavity effect. Secondly, the experimental design included the features of second generation Mercury-Cadmium-Telluride (MCT) cooled detectors with lower instrumental noises and finer channels. Thirdly, as opposed to previous studies that used predefined spectral configurations to determine the most suited one, we conducted an optimization of the spectral configuration by crossing, on a pair basis, several positions of the four TIR channels over a range of wavelengths. Fourthly, we quantified the TES sensitivity to atmospheric perturbations, by comparing LST retrievals with and without atmospheric noise.

*Corresponding author at : 5 Esp Compans Caffarelli, 31000 Toulouse, France.
Email address: thomas.vidal@acri-st.fr (Thomas H. G. Vidal)

We observed an overall moderate sensitivity of TES LST retrievals to the spectral channel positions, with a maximum RMSE variation of 0.31 K within the atmospheric spectral windows. Furthermore, the TES method was sensitive to three main parameters, namely the instrumental noise, the atmospheric downwelling irradiance, and the transmittance due to ozone and water vapor, with RMSEs larger than 1 K for specific channel locations. Moreover, by considering possible superimposition of two channels, we noted that the TES method could achieve similar performance by considering three or four channels. Eventually, our study enabled us to recommend a new spectral configuration for the TRISHNA TIR instrument, that is more robust to atmospheric perturbations and to uncertainties on channel positions and bandwidths.

Keywords: Thermal infrared remote sensing, Satellite mission design, Spectral channels positioning, Temperature/emissivity separation, Vegetation canopy - scaled cavity effects, Mercury - Cadmium - Telluride cooled detectors, Atmospheric corrections, Sensitivity analysis

1. Introduction

The increasing need for efficient satellite retrieval of land surface temperature (LST) has become unanimous in the global scientific community (Murphy, 2006; Malenovsky et al., 2012; Lagouarde et al., 2013; Weiss et al., 2020). Indeed, LST is a key parameter in environmental physics, since it drives numerous land surface processes such as radiation budgets (Hulley and Hook, 2010; Mira et al., 2016; Ogawa et al., 2002, 2003; Yan et al., 2020), water depletion from soils through evapotranspiration (Bigéard et al., 2019; Carlson and Petropoulos, 2019; French et al., 2005; Galleguillos et al., 2011, 2010; Gómez et al., 2005; Jacob et al., 2002; Montes et al., 2014; Montes and Jacob, 2017; Pardo et al., 2014; Vinukollu et al., 2011), photosynthesis and soil respiration (Bayat et al., 2018; Inoue et al., 2004; Olioso et al., 2005), and it can be linked to paramount environmental processes such as pollutant degradation (Louchart and Voltz, 2007) and pathogen dissemination (Courault et al., 2009; Schröder et al., 2006;

15 Sobrino et al., 2016).

16 The consensus on the need for satellite-based LST retrievals is notably illus-
17 trated by a recent soar of related satellite projects, with the launch in 2018 of the
18 NASA ECOsystem Spaceborne Thermal Radiometer Experiment onboard the
19 International Space Station (ECOSTRESS, Hulley et al., 2017), the ESA future
20 High Spatio-Temporal Resolution Land Surface Temperature Mission (HSTR
21 LSTM, Koetz et al., 2018), and the CNES (French spatial agency) / ISRO (In-
22 dian Space Research Organisation) cooperation project on the Thermal infraRed
23 Imaging Satellite for High-resolution Natural resource Assessment mission (TR-
24 ISHNA, Lagouarde et al., 2018).

25 The TRISHNA satellite will embark both a visible/short wave infrared and a
26 thermal infrared (TIR) sensor. With that payload, the TRISHNA mission will
27 focus on six monitoring scientific objectives, addressing 1/ energy and water
28 budgets of the continental biosphere in relation to ecosystem stress and water
29 use, 2/ coastal and inland waters, 3/ climatology and fluxes within urban areas
30 in relation to urban heating environments, 4/ geological phenomena such as
31 volcanoes or earthquakes in relation to solid Earth, 5/ cryospheric processes
32 such as snowmelt and related runoff, and 6/ atmospheric characterization (e.g.,
33 water vapor). The two first objectives are the design drivers, with an emphasis
34 on ecosystem stress and water use monitoring. In a climate change context, the
35 latter is a critical aspect of the mission, notably for inter-tropical regions such
36 as India, for sub-humid southern France regions, or for semi-arid to arid regions
37 of the Mediterranean basin.

38 In order to efficiently reach the objectives of the TRISHNA mission, the
39 platform will be set to an approximately 760 km orbit with a 1,000 km swath
40 $\pm 34^\circ$ FOV), which allows a ~ 60 m nadir spatial resolution and a 3-days revisit
41 time for global coverage (Lagouarde et al., 2019). These mission parameters
42 are critical since they will allow precise monitoring of, for instance, water stress
43 at crop field scale or urban heat islands. In order to guarantee such a precise
44 monitoring, another important mission parameter is the allocation of 4 channels
45 between 8 and 12 μm for the thermal infrared sensor. These four channels are

46 implemented by using second generation Mercury-Cadmium-Telluride (MCT)
47 cooled detectors with better instrumental performance (lower noises and finer
48 channels) than first generation microbolometers used on board previous satellite
49 missions. In this configuration, high quality TRISHNA level 2 products are
50 expected to be available to the community every 12 h.

51 In order to ensure precise measurements, suitable methods shall be used to
52 retrieve LST from out-of-sensor TIR radiances. The retrieval issue lies in the
53 fact that radiances in the TIR domain (7.5-13 μm) depend on both temperature
54 and emissivity of the observed surface. Hence, even with proper atmospheric
55 corrections, the problem of retrieving these surface variables is ill-posed be-
56 cause of a larger number of unknowns (N_B emissivities + 1 temperature), than
57 measurements (N_B radiances), with N_B the number of TIR spectral channels.

58 Among the existing methods for LST retrieval (see Dash et al., 2002; Jacob
59 et al., 2008; Li et al., 2013, for reviews on the matter), the best fitted for the
60 TRISHNA objectives is the Temperature-Emissivity Separation method (TES,
61 Gillespie et al., 1998), notably because it does not require ancillary information
62 on the observed scene and can directly produce LST estimates for each satel-
63 lite overpass, provided that prior atmospheric corrections are conducted. This
64 method was developed specifically for TIR multispectral precursor sensors such
65 as the spaceborne Advanced Spaceborne Thermal Emission and Reflection Ra-
66 diometer (ASTER) sensor or the airborne TIMS (Thermal Infrared Multispec-
67 tral Scanner) sensor, and later on analysed or modified in order to stabilize and
68 enhance its performance (Mira et al., 2009; Coll et al., 2007; French et al., 2008;
69 Gillespie et al., 1999; Göttsche and Hulley, 2012; Grigsby et al., 2015; Gustafson
70 et al., 2006; Hulley et al., 2008, 2012; Jacob et al., 2004, 2017; Schmugge et al.,
71 1998, 2002; Zheng et al., 2019).

72 The second alternative for LST estimation in the context of the TRISHNA
73 mission is the Split Window (SW) method, notably because it permits to se-
74 cure the operational delivery of LST retrievals in case of failure of at most two
75 channels, and is more easily applicable than the TES method as it does not
76 require prior atmospheric correction. It can even ensure better LST results for

77 grey-body observations, *i.e.*, scenes with low spectral contrast (see Li et al.,
78 2013, for an overview of the existing SW methods). Eventually, the SW method
79 could be operationally used with retrievals of land surface emissivity and at-
80 mospheric water vapor content, which should be indirectly obtained from the
81 TRISHNA VIS/NIR instrument via a NDVI-based method (Neinavaz et al.,
82 2020; Vanhellemont, 2020; Jiménez-Muñoz and Sobrino, 2006; Sobrino et al.,
83 2004; Olioso, 1995) and via a so-called 'water vapor channel' at $0.910 \mu\text{m}$, re-
84 spectively.

85 As an important step of the TRISHNA mission preparation for high quality
86 observations, the TES and SW methods require prior optimization of the in-
87 strument spectral configuration based on performance analyses. This consists in
88 establishing the locations and bandwidths of the spectral channels, namely two
89 channels between 10 and $12 \mu\text{m}$ for SW, combined with two additional channels
90 between 8 and $9.5 \mu\text{m}$ for TES, so that: 1/ atmospheric perturbations are en-
91 hanced locally (for SW) or minimized overall (for TES), 2/ emissivity contrast
92 is spectrally minimized (for SW) or maximised (for TES), and 3/ instrumental
93 noises are reduced (for both TES and SW).

94 Pioneer work in that regard was conducted by Caselles et al. (1998), who
95 tested the performance of a SW method for several 2-channels configurations in
96 the context of the PRISM satellite development. Thanks to enhanced numeri-
97 cal capabilities, further studies evaluated the performances of the TES and SW
98 methods for a larger number of spectral configurations (Sobrino et al., 2010;
99 Sobrino and Jiménez-Muñoz, 2014). In order to propose a spectral configu-
100 ration for the MICRO SATELLITE for THERMAL INFRARED GROUND surface IMAGING
101 (MISTIGRI) mission (Lagouarde et al., 2013), Jacob et al. (2021) examined
102 the performance of the TES method for six spectral configurations based on
103 microbolometer detectors. For this study, they used a representative emissivity
104 spectra dataset proposed by Jacob et al. (2017) to account for the cavity effect,
105 since the latter results in an upper (respectively lower) shift in emissivities (re-
106 spectively radiometric temperature) as compared to the original TES settings.
107 Using the same emissivity dataset, and in order to propose a spectral config-

108 uration dedicated to the SW method for the TRISHNA mission, Vidal et al.
109 (2021) developed a bi-dimensional optimization approach that simultaneously
110 moves spectral channels rather than using predefined configurations.

111 In order to define an optimal spectral configuration, the current study aims
112 at conducting a sensitivity analysis of the TES method to the position of the
113 four TRISHNA spectral channels. It capitalizes on the contributions discussed
114 above, since it addresses the design of a TRISHNA-TES dedicated configura-
115 tion 1/ by including the features of second generation MCT cooled detectors,
116 2/ by accounting for cavity effects in vegetation canopy, 3/ by conducting a sen-
117 sitivity analysis that simultaneously moves spectral channels rather than using
118 predefined configurations, and 4/ by using an end-to-end simulator that includes
119 sensor measurements, atmospheric corrections and the TES retrieval procedure.

120 We first present a description of the TES method in § 2, since it is the main
121 object of our study. Then we describe the end-to-end simulator we specifically
122 developed for this work in § 3, as well as its implementation in the context of
123 TRISHNA studies in § 4. The experimental plan of our sensitivity analysis is
124 described in § 5, and § 6 details the various results obtained, which are then
125 discussed in § 7. We conclude in § 8 with limitations and opportunities of the
126 work to date.

127 **2. The Temperature/Emissivity Separation (TES) method**

128 *2.1. TES principle and overview*

129 The TES method (Gillespie et al., 1998) was initially developed by the
130 ASTER Temperature Emissivity Working Group (hereafter TEWG) in order
131 to efficiently tackle the issue of surface temperature/emissivity separation (§ 1).
132 After a thorough study of existing temperature and/or emissivity retrieval meth-
133 ods, TES was proposed by combining key features of previous methods, espe-
134 cially the Normalized Emissivity Method (NEM, Realmuto, 1990) and Minimum-
135 Maximum Difference method (MMD, Matsunaga, 1994). More particularly, in
136 order to render the temperature/emissivity separation issue deterministic, the

137 TES method is based on the idea that over $N_B \geq 3$ channels in the TIR domain,
138 the emissivity spectrum of a natural surface contains at least one value close
139 to unity. From this hypothesis, a first estimation of the surface temperature
140 and iterative sky irradiance correction is conducted by the NEM module. From
141 this correction a first emissivity spectrum is derived and ratioed to its mean
142 value, resulting in an relative emissivity spectrum that has the shape but not
143 the amplitude of the observed spectrum. This amplitude is then found within
144 the MMD module by relating the minimum emissivity to the spectral contrast,
145 which notably implies that the used spectral channels allow an efficient measure-
146 ment of the latter. Eventually, a more correct final temperature is calculated
147 from the maximum emissivity value.

148 The ASTER TEWG and following studies have shown that TES can re-
149 trieve surface emissivities within an 0.01 error margin (Coll et al., 2003) and
150 temperature within a 1 K error margin (Schmugge et al., 2003), assuming well
151 calibrated and accurate radiometric measurements. This error margin is satis-
152 factory for the TRISHNA mission, which instrumental specification on absolute
153 calibration accuracy is about 0.7 K, for a required precision on LST of ~ 1.5 K
154 (Lagouarde et al., 2019). Note that recently, Zheng et al. (2019) have suc-
155 cessfully enhanced the TES method by proposing a SW/TES hybrid method
156 that reduces the TES precision to 0.87 K. However, their method is based on
157 a dry-atmosphere hypothesis, which is not relevant for our study, since most of
158 the regions of interest for the TRISHNA mission, such as inter-tropical regions,
159 sustain a humid climate. The TES processing flow is hereafter detailed.

160 *2.1.1. NEM module*

161 Using as input surface-leaving radiance $L_i^{sur\uparrow}$, which necessitates to apply
162 atmospheric corrections to the out-of-sensor (OS) radiance before entering the
163 TES method, the role of the NEM module is threefold:

- 164 1. to retrieve a first estimate for the surface temperature;
- 165 2. to estimate the shape for the emissivity spectrum;

166 3. to iteratively correct for the atmospheric downwelling irradiance impact
 167 on surface radiance.

168 It is first supposed that the anisotropic behavior of the surface is neglected,
 169 and that the emissivities are all equal to a given maximum emissivity close
 170 to unity $(\varepsilon_i)_{i \in [1; N_B]} = \varepsilon_{max} = 0.99$, typical of vegetated surfaces, snow and
 171 water. The ground emitted radiance L_i^{em} can then be estimated from the
 172 known surface-leaving radiance $L_i^{sur\uparrow}$ and the atmospheric downwelling irra-
 173 diance $E_i^{atm\downarrow}$ via:

$$L_i^{em} = L_i^{sur\uparrow} - (1 - \varepsilon_{max}) \frac{E_i^{atm\downarrow}}{\pi} \quad (1)$$

174 The NEM temperature T_{NEM} is then calculated as the maximum temper-
 175 ature obtained from each ground emitted radiance L_i^{em} via inverse Planck's
 176 law:

$$T_i = B^{-1} \left(\frac{L_i^{em}}{\varepsilon_{max}}, \lambda_i \right) \quad (2)$$

$$T_{NEM} = \max(T_i) \quad (3)$$

$$B^{-1}(L_i, \lambda_i) = \frac{c_2}{\lambda_i \ln \left(\frac{c_1}{\pi \lambda_i^5 L_i} + 1 \right)} \quad (4)$$

177 where c_1 and c_2 are the radiative constants respectively equal to $3.74151 \times$
 178 10^{-16} W.m⁻² and 0.0143879 m.K. T_{NEM} is indeed most likely to be the best
 179 estimate of the actual surface temperature in presence of uncorrected effects
 180 of the atmospheric irradiance. Afterwards, the NEM emissivity spectrum is
 181 calculated as the ratio between the calculated ground emitted radiance L_i^{em}
 182 and that of a blackbody at the NEM temperature:

$$\varepsilon_{NEM,i} = \frac{L_i^{em}}{B(T_{NEM}, \lambda_i)} \quad (5)$$

183 where $B(T_{NEM}, \lambda_i)$ is the Planck's law associated to the surface temperature
 184 T_{NEM} at the channel effective wavelength λ_i :

$$B(T, \lambda) = \frac{c_1}{\lambda^5 \pi \left[\exp \left(\frac{c_2}{T\lambda} \right) - 1 \right]} \quad (6)$$

185 The obtained emissivity spectrum is then used to re-estimate L_i^{em} with Equa-
 186 tion 1, and the process from Equation 1 to 5 is repeated until convergence or
 187 until the number of iteration reaches an arbitrary threshold $N_{it}^{max} = 12$. The
 188 convergence condition is satisfied if the change in L_i^{em} between steps is lower
 189 than a given threshold t_2 , which is currently set to its ASTER value of 0.05
 190 $\text{W.m}^{-2}.\text{sr}^{-1}.\mu\text{m}^{-1}$ and shall be refined for TRISHNA to its Noise Equivalent
 191 Delta Radiance ($\text{Ne}\Delta L$) value. Divergence is also tested by calculating the sec-
 192 ond derivative of L_i^{em} versus the number of iterations N_{it} , *i.e.*, its variation
 193 rate. If this rate exceeds a threshold t_1 , $|\Delta^2 L_i^{em} / \Delta N_{it}^2| > t_1$, TES is halted
 194 and the last T_{NEM} and $\varepsilon_{NEM,i}$ values are returned along with an error flag.
 195 The threshold t_1 is also set to its ASTER original value, which is the same
 196 as t_2 , and should be refined during the future TRISHNA level-2 study. Be-
 197 cause the TRISHNA mission will mainly focus on ecosystems, and therefore
 198 surface emissivities greater than 0.5, TES can also be aborted in the case where
 199 one of the NEM calculated emissivities exceeds reasonable limits, thus set to
 200 $0.5 < \varepsilon_{NEM,i} < 1.0$. Once convergence is reached, further ε_{max} refinement is
 201 conducted, notably by evaluating the variance of the $\varepsilon_{NEM,i}$ values obtained.
 202 If the variance is larger or lower than a given threshold, the pixel is consid-
 203 ered to be composed mainly of rocks and soils, or of near graybody surfaces,
 204 respectively. The ε_{max} refinement process used in this study is the same as de-
 205 scribed in Gillespie et al. (1998). Note that the aforementioned tests and flags
 206 are paramount in terms of mission requirements, since they will allow to define
 207 confidence levels on the results of the method for each pixel.

208 2.1.2. Ratio module

209 In the ratio module the relative emissivities β_i are calculated as the ra-
 210 tio between the NEM-obtained emissivities and their average value on the N_B
 211 channels:

$$\beta_i = \frac{\varepsilon_{NEM,i}}{\bar{\varepsilon}} = N_B \cdot \varepsilon_{NEM,i} \left(\sum_i \varepsilon_{NEM,i} \right)^{-1} \quad (7)$$

212 *2.1.3. MMD module*

213 The aim of the MMD module is to rescale the relative emissivity spectrum
 214 $(\beta_i)_{i \in [1; N_B]}$ to an actual emissivity spectrum $(\varepsilon_i^{MMD})_{i \in [1; N_B]}$ using the MMD
 215 (\equiv spectral contrast) of the $(\beta_i)_{i \in [1; N_B]}$. This is achieved by linking the MMD
 216 to the minimum emissivity ε_{min} of the original spectrum using an empirically-
 217 determined relationship (Matsunaga, 1994). The ε_{min} is afterwards used to scale
 218 the relative emissivity spectrum. For that purpose, the MMD is first calculated
 219 as:

$$\text{MMD} = \max_i(\beta_i) - \min_i(\beta_i) \quad (8)$$

220 and then linked to the minimum emissivity ε_{min} via:

$$\varepsilon_{min} = A - B \cdot \text{MMD}^C \quad (9)$$

221 where A, B and C are coefficients which depend upon the Instrumental Spectral
 222 Response Function (ISRF) of the TIR sensor to be used, which are obtained
 223 from a regression using a representative emissivity spectra database. Finally,
 224 the β_i values can be rescaled to the emissivity spectrum following:

$$\varepsilon_i^{TES} = \frac{\varepsilon_{min}}{\min_i(\beta_i)} \beta_i \quad (10)$$

225 The final surface temperature T_{sur}^{TES} is then computed by conducting a last
 226 NEM iteration (equations (1) to (3)), using the estimated surface emissivity
 227 spectrum $(\varepsilon_i^{TES})_{i \in [1; N_B]}$. A summary of the TES method described above can
 228 be found in Figures 2 and 3 of Gillespie et al. (1998).

229 **3. PERSEUS description**

230 In this section, we present the end-to-end simulator that we designed and
 231 implemented for our study, which aims to optimize the spectral configuration
 232 of the TRISHNA TIR instrument when used with the TES method. Here we
 233 provide an overview of the simulator, along with descriptions of each related
 234 module.

235 *3.1. PERSEUS overview*

236 For the purpose of this study, an end-to-end simulator named PERSEUS
 237 (Python End-to-end Remote SENSing instrUMENT Simulator) has been devel-
 238 oped. Indeed, it was necessary to use a modular, versatile and fast-computing
 239 simulator, since a large number of simulations were conducted. As such, PERSEUS
 240 can simulate top-of-atmosphere (TOA) and out-of-sensor (OS) radiances from
 241 any set of driving factors related to observation conditions, the latter including
 242 surface temperature T_{sur} and emissivity spectrum (ε_λ), atmospheric parameters
 243 (downwelling irradiance, upwelling radiance, transmittance), and the spectral
 244 configuration of the considered TIR sensor (response function for each of the
 245 N_B channels, so-called ISRF). Applying the inversion procedure to the obtained
 246 OS radiances then permits to retrieve the surface properties of interest, namely
 247 T_{sur} and channel emissivities $(\varepsilon_i)_{i \in [1; N_B]}$. The retrieved values can afterwards
 248 be compared to their input counterparts in order to conduct performance analy-
 249 ses, provided reference emissivity spectra are convolved with the ISRF. Figure 1
 250 displays a schematic overview of PERSEUS and its three modules: the radi-
 251 tive transfer module, the instrument module and the inversion module. These
 252 modules are presented in the following subsections.

253 *3.2. The radiative transfer module*

254 The PERSEUS radiative transfer module uses the IDL-encoded COMANCHE
 255 radiative transfer tool (Poutier et al., 2002) which has been adapted to use
 256 MODTRAN 5.2 (Berk and Anderson, 2008). It allows the calculation, within
 257 the TIR spectral domain, of atmospheric parameters and TOA radiance, from
 258 the scene surface variables T_{sur} and (ε_λ) , for a given atmospheric profile. The
 259 TOA radiance is calculated via:

$$L_\lambda^{sur\uparrow} = \varepsilon_\lambda B(T_{sur}, \lambda) + (1 - \varepsilon_\lambda) \frac{E_\lambda^{atm\downarrow}}{\pi} \quad (11)$$

$$L_\lambda^{TOA} = \tau_\lambda^{atm} L_\lambda^{sur\uparrow} + L_\lambda^{atm\uparrow} \quad (12)$$

260 where $L_\lambda^{sur\uparrow}$ and $L_\lambda^{atm\uparrow}$ are the surface leaving radiance and atmospheric up-
 261 welling radiance, respectively, $E_\lambda^{atm\downarrow}$ is the atmospheric downwelling irradiance,

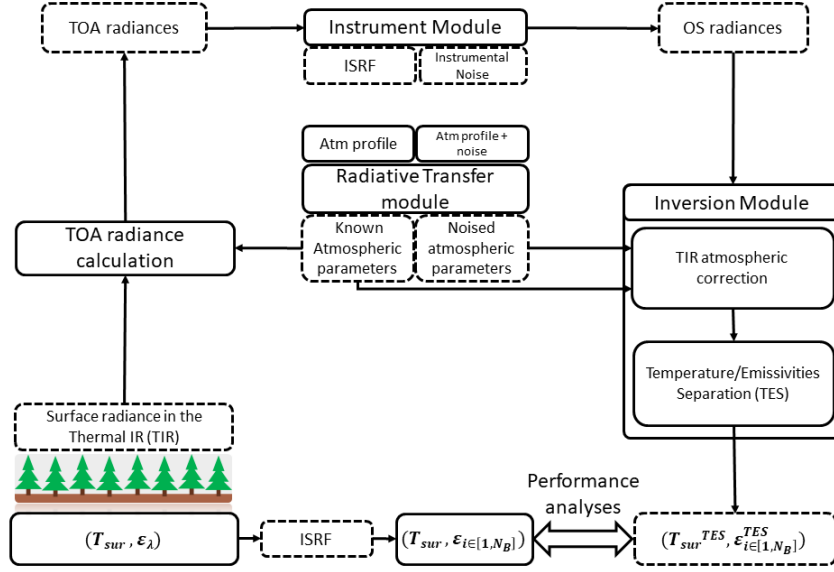


Figure 1: Schematic overview of PERSEUS and its three modules : the radiative transfer module, the instrument module and the inversion module. The variables calculated by the simulator are highlighted in dotted lines.

262 L_{λ}^{TOA} is the TOA radiance, and τ_{λ}^{atm} is the atmospheric transmittance between
 263 the sensor and the target.

264 3.3. The instrument module

265 The aim of the PERSEUS instrument module is to account for the signal
 266 modifications applied to the TOA radiance by the TIR sensor, which eventually
 267 permits to obtain the OS radiance. These within-sensor signal modifications
 268 consist in applying the ISRF and instrumental noises.

269 3.3.1. ISRF application

270 Upon entering the instrument module, the total TOA radiance $L^{TOA}(\lambda)$,
 271 with λ the wavelength, is convolved with the spectral response function $S_i(\lambda)$
 272 of each of the N_B channels, in order to obtain the equivalent TOA radiance in

273 channel i , L_i^{TOA} :

$$L_i^{TOA} = \frac{\int_{\lambda_{min,i}}^{\lambda_{max,i}} L^{TOA}(\lambda) \cdot S_i(\lambda) \cdot d\lambda}{\int_{\lambda_{min,i}}^{\lambda_{max,i}} S_i(\lambda) \cdot d\lambda} \quad (13)$$

274 where $\lambda_{min,i}$ and $\lambda_{max,i}$ are the limit wavelengths of channel i . It should be
 275 noted that the PERSEUS ISRF module can be used to apply the ISRF on any
 276 spectral variable, such as the prescribed emissivity spectra (ε_λ).

277 3.3.2. Applying instrumental noises

278 In order to determine the radiance equivalent noise on each channel $Ne\Delta L_i$,
 279 PERSEUS uses the following noise model:

$$Ne\Delta L_i = \sqrt{a_i + b_i \cdot L_i} \quad (14)$$

280 where the term a includes the quantification noise and the dark current noise,
 281 while the term bL_i refers to the shot noise modelled by a Poisson process. Once
 282 the $Ne\Delta L_i$ is calculated, the corresponding instrumental noises are applied to
 283 each channel i as a white Gaussian noise with a standard deviation of $\sigma =$
 284 $Ne\Delta L_i$:

$$L_i^{OS} = L_i^{TOA} + \mathcal{N}(0, \sigma = Ne\Delta L_i) \quad (15)$$

285 where L_i^{OS} is the OS radiance in any of the N_B channels i .

286 3.4. The inversion module

287 The PERSEUS inversion module includes the TES method with prior atmo-
 288 spheric corrections. As depicted in Figure 1, the atmospheric corrections can be
 289 conducted considering reference or noised atmospheric parameters, where the
 290 latter permit to account for uncertainties on atmospheric corrections. Noised
 291 atmospheric parameters are obtained by adding Gaussian white noise at each
 292 level of any atmospheric profile of temperature, relative humidity and ozone con-
 293 tent, before entering the radiative transfer module (§ 3.2), by using the following
 294 procedure:

- 295 • for the atmospheric temperature, a white Gaussian noise with a standard
296 deviation of 0.8 K is added, as suggested by Barsi et al. (2003);
- 297 • for the relative humidity (RH) and the ozone concentration ($[O_3]$), white
298 Gaussian noises with respective standard deviations of $0.1 \times RH$ and $0.2 \times$
299 $[O_3]$ error are added, as suggested by Palluconi et al. (1999).

300 The outputs of the radiative transfer simulations conducted with these noised
301 profiles are used to derive the atmospheric parameters of interest, namely at-
302 mospheric upwelling radiance $L_i^{atm\uparrow}$, atmospheric transmittance τ_i^{atm} and at-
303 mospheric downwelling irradiance $E_i^{atm\downarrow}$. These atmospheric parameters are
304 then used to conduct atmospheric corrections by computing the surface-leaving
305 radiances $L_i^{sur\uparrow}$ within each of the N_B channels i , following:

$$L_i^{sur\uparrow} = \frac{L_i^{OS} - L_i^{atm\uparrow}}{\tau_i^{atm}} \quad (16)$$

306 In the atmospheric noise-free case, atmospheric corrections rely on the out-
307 puts of radiative transfer simulations obtained from the original atmospheric
308 profiles. Eventually, once the surface-leaving radiance $L_i^{sur\uparrow}$ is obtained, the
309 TES method is applied to the N_B surface-leaving radiances $L_i^{sur\uparrow}$, while using
310 the atmospheric downwelling irradiance $E_i^{atm\downarrow}$ (§ 2).

311 3.5. Performance analysis

312 Once the surface temperatures T_{sur}^{TES} are estimated, they can be directly
313 compared with their input counterparts, to assess the performance of the TES
314 method for the retrieval of surface temperature and emissivity. The obtained
315 emissivities $(\varepsilon_i^{TES})_{i \in [1; N_B]}$ are compared against the ISRF-convolved surface
316 emissivity spectra $(\varepsilon_i)_{i \in [1; N_B]}$. The latter are obtained by applying the ISRF of
317 the instrument to the prescribed surface emissivity spectra (ε_λ) .

318 It should be noted that the bandpass resampling of spectral values obtained
319 by convolution with the ISRF is expected to add errors on the LST and LSE
320 retrievals (Richter and Coll, 2002; Jiménez-Muñoz and Sobrino, 2006). However,
321 as discussed in Jiménez-Muñoz and Sobrino (2006), this can not be avoided

322 in end-to-end simulations study such as ours. Moreover, as we study relative
323 performances of various spectral configurations, and not absolute performances,
324 these effects should not significantly change our conclusions.

325 **4. PERSEUS implementation in the context of the TRISHNA mis-** 326 **sion**

327 For our study, we ran various simulations of TRISHNA measurements over
328 a wide range of surface and atmospheric conditions. In the current section we
329 present the datasets we used for characterizing the surface conditions (emissivity
330 spectra, temperature) and the atmospheric conditions (variable profiles) of the
331 pixel-sized scenes, along with the PERSEUS implementation used to obtain a
332 representative dataset of TOA radiances.

333 *4.1. The surface emissivity spectra dataset*

334 We select the emissivity dataset simulated by Jacob et al. (2017) with the
335 SAIL-Thermique model (Oliosio, 1995; Oliosio et al., 2018), and previously used
336 to design the spectral configuration of the MISTIGRI TIR sensor (Jacob et al.,
337 2021). This dataset, hereafter labelled SAIL271, comprises 271 simulated emis-
338 sivity spectra of vegetation canopies over soils. It was implemented in order
339 to form a realistic and representative dataset of land surface emissivity spec-
340 tra, dedicated to TIR studies. Indeed, the simulated emissivity spectra account
341 for radiance trapping within canopy and its subsequent cavity effect, and are
342 representative of a large range of soil and plant conditions, notably for Leaf
343 Area Index (LAI) and Average Leaf Angle (ALA). Among the 63,700 original
344 emissivity spectra simulated by considering a wide range of soil reflectance and
345 leaf reflectance / transmittance, the final 271 spectra were selected by using the
346 Spectral Angle Mapper method (SAM, Girouard et al., 2004). All the emissivity
347 spectra of the SAIL271 dataset were obtained considering a nadir viewing di-
348 rection, because 1/ angular variation of canopy emissivity is low between nadir
349 and 40° (Oliosio, 1995; Guillevic et al., 2003; Ren et al., 2015) although it can

Table 1: Summary of the soil and plant conditions taken into account in the SAIL271 dataset (from Jacob et al., 2017).

Parameters	Values
LAI	0, 0.25, 0.5, 1, 2, 4, 7
ALA	15°, 35°, 55°, 75°
View zenith angle	Nadir

reach 0.01 over row-structured canopies (Sobrino and Caselles, 1990; Sobrino et al., 2005), and 2/ the view zenith angle of the TRISHNA sensor is lower than 34°. A summary of the range of these parameters is displayed in Table 1, and a detailed description on the elaboration of the dataset can be found in Jacob et al. (2017). The SAIL-Thermique model describes vegetation canopy as a simple homogeneous volume of turbid medium, which induces errors when considering most of continental surfaces with heterogeneous and discontinuous canopies. According to the few comparison studies that are reported for emissivity models (Sobrino et al., 2005; Cao et al., 2018), resulting errors can reach up to 0.005 over large ranges of LAI (0 to 7) and of view zenith angle (0 to 50°).

4.2. The atmospheric profiles dataset

In order to work with a representative dataset of atmospheric profiles, we use the TIGR database that contains 2311 atmospheric profiles statistically selected over 80 000 radiosonde based records (Chevallier et al., 2000). We characterize these 2311 profiles by considering two main drivers of the atmospheric radiative transfer in the TIR spectral domain, namely the atmospheric water vapor content (AWVC) and the equivalent atmospheric temperature T_{eq}^{atm} . The AWVC drives the atmospheric transmittance, and is defined as (Jacob et al., 2003):

$$AWVC = \int_0^{z_{max}} \rho_v(z) dz \quad (17)$$

where z_{max} is the highest altitude of the atmospheric profile, and ρ_v the water vapor density. T_{eq}^{atm} drives the atmospheric emission, and therefore $E^{atm\downarrow}$ and

370 $L^{atm\uparrow}$. It is defined as:

$$T_{eq}^{atm} = \frac{\int_0^{z_{max}} T(z) \cdot \rho_v(z) \cdot dz}{\int_0^{z_{max}} \rho_v(z) \cdot dz} \quad (18)$$

371 In order to reduce the computational time, the TIGR dataset is filtered by
372 comparing the 2311 profiles to each other, and by keeping those that meet the
373 following conditions:

- 374 1. the difference between atmospheric water vapor content AWVC is larger
375 than 0.15 g.cm^{-2} ;
- 376 2. the difference between equivalent atmospheric temperatures T_{eq}^{atm} is larger
377 than 5 K.

378 These threshold values are empirically selected in order to obtain a number
379 of profiles consistent with our numerical capabilities, while conserving the enve-
380 lope of the atmospheric profile distribution. The subsequent filtering results in a
381 selection of 24 atmospheric profiles. Figure 2 displays the original (Figure 2(a))
382 and reduced (Figure 2(b)) atmospheric profile datasets in the $T_{eq}^{atm} / \text{AWVC}$
383 space. It shows that the reduced dataset preserves the envelope of the atmo-
384 spheric profile distribution. However, the density of the atmospheric profiles is
385 homogenized in the reduced dataset as compared to the original one. Indeed,
386 the original dataset contains a larger number of dry atmospheres ($\text{AWVC} < 2.5$
387 g.cm^{-2}) than wet ones ($\text{AWVC} \geq 2.5 \text{ g.cm}^{-2}$), whereas the reduced dataset con-
388 tains 13 wet and 11 dry atmospheres. Nevertheless, this new distribution fits
389 with the context of our study, since it accounts for wet atmospheres corre-
390 sponding to tropical latitudes, the latter being of paramount interest for the
391 TRISHNA mission. The effect of this atmospheric profile selection on both the
392 TES performance and the representativeness of the results in the context of the
393 TRISHNA mission will be discussed in § 7. Note that the reduced dataset of
394 atmospheric profiles is hereafter labelled TIGR24.

395 4.3. TOA radiance simulations

396 Once the SAIL271 and TIGR24 datasets are obtained, and in order to take
397 into account realistic surface/air temperature gradients, each surface emissivity

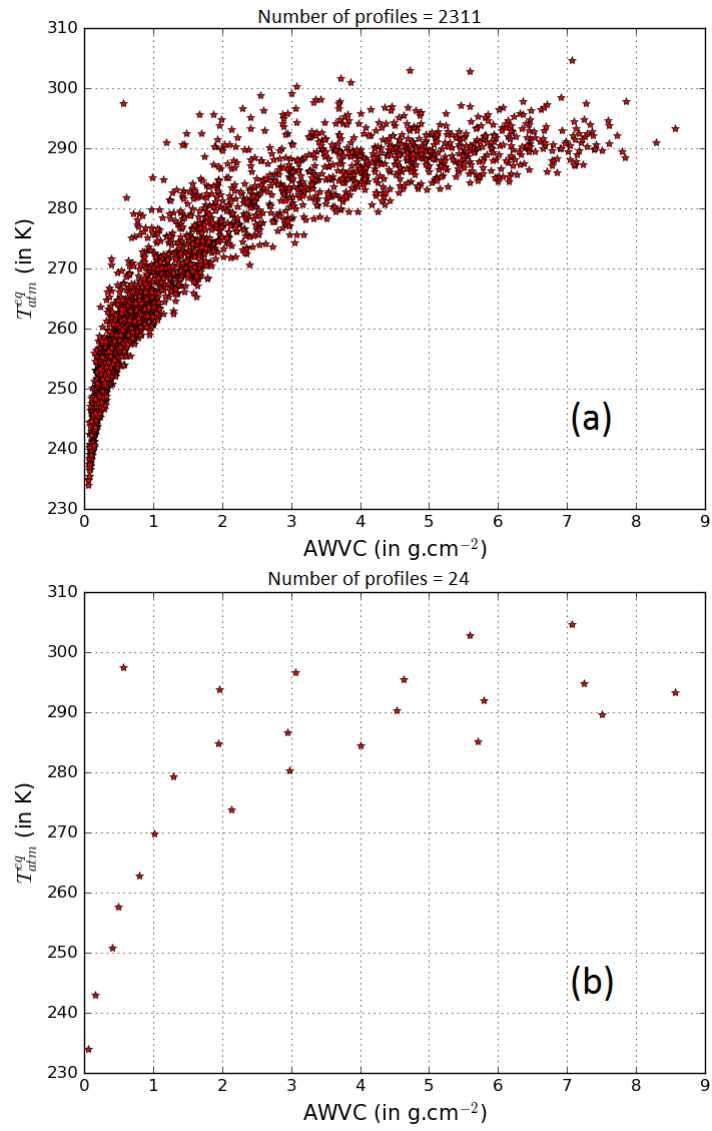


Figure 2: Representation of the atmospheric profiles in the T_{eq}^{atm}/AWVC plane for (a) the complete TIGR dataset, and (b) the TIGR24 one.

398 spectrum/atmospheric profile combination is associated to five surface temper-
399 atures following $T_{sur} = [T_{skin} - 5\text{K}; T_{skin}; T_{skin} + 5\text{K}; T_{skin} + 10\text{K}; T_{skin} + 15\text{K}]$,
400 where T_{skin} is the temperature at the lower level of the corresponding atmo-
401 spheric profile. The $271 \times 24 \times 5 = 32,520$ PERSEUS simulations are then
402 carried out in order to calculate the TOA radiances at nadir viewing direction,
403 for each possible combination of surface emissivity spectra/atmospheric pro-
404 file/surface temperature. This results in a dataset of TOA radiances which is
405 structurally representative of a wide range of realistic situations.

406 5. Setup for the sensitivity analysis

407 In this section we first present the reference TRISHNA instrumental configu-
408 ration, including both the ISRF $S_i(\lambda)$ and the Noise Equivalent Delta Radiance
409 $\text{Ne}\Delta L_i$ for each channel i . Next, we describe the sensitivity analysis based
410 on the changes in TES performance when moving the spectral channels. Fi-
411 nally, we expose the methodological design for addressing the robustness of the
412 TRISHNA reference spectral configuration to uncertainties on ISRF due to in-
413 strumental design, namely uncertainties on channel position and full width at
414 half maximum (FWHM).

415 5.1. TRISHNA reference instrumental configuration

416 The TRISHNA mission group set a baseline for the four spectral channels
417 of the TIR sensor, which theoretically allows a comfortable trade-off between
418 good performance of LST-retrieval methods and mission cost. Table 2 and Fig-
419 ure 3 detail the central wavelength and FWHM for each of the four TRISHNA
420 spectral channels, labelled respectively TIR1, TIR2, TIR3 and TIR4. The four
421 TRISHNA TIR channels are pair-distributed on either side of the ozone ab-
422 sorption feature spiking at $9.7 \mu\text{m}$, with TIR1 and TIR2 below and TIR3 and
423 TIR4 above. Moreover, water vapor absorption defines the atmospheric window
424 within which the four channels are located, with low atmospheric transmittance
425 below $8.25 \mu\text{m}$ and above $12.5 \mu\text{m}$. The aforementioned ozone and water vapor

Table 2: Central wavelength λ_c and FWHM for the TRISHNA reference channels.

	TIR1	TIR2	TIR3	TIR4
λ_c (μm)	8.6	9.1	10.4	11.6
FWHM (μm)	0.35	0.35	0.7	1.0

Table 3: Instrumental noise parameters for the TRISHNA reference channels.

	TIR1	TIR2	TIR3	TIR4
a_i ($10^{-5} W^2.m^{-4}.sr^{-2}.\mu m^{-2}$)	18.3	16.3	4.47	4.32
b_i ($10^{-8} W.m^{-2}.sr^{-1}.\mu m^{-1}$)	411	547	8.13	175

426 absorption features are expected to be the main constraining factors for channel
 427 positioning.

428 The values of the a and b parameters used in our study for the calculation
 429 of the $Ne\Delta L_i$, as described in § 3.3.2, are given in Table 3. These values were
 430 provided by CNES as first estimates of the TRISHNA instrumental noises. As
 431 expected with regards to their smaller FWHM, the noises on TIR1 and TIR2
 432 are significantly larger than those on TIR3 and TIR4.

433 5.2. ISRF variations for the sensitivity analysis

434 The aim of this study is to define the best spectral configuration for the
 435 TRISHNA TIR sensor. Therefore, the main task is to evaluate the effects of
 436 changes in channel positions, *i.e.*, changes on the central wavelength λ_c of each
 437 TIR channel. In order to do so, the TIR1/TIR2 and TIR3/TIR4 pairs are stud-
 438 ied separately. For each pair of channels, we conduct the sensitivity analysis by
 439 considering simultaneous variations of both channels. This separation of chan-
 440 nels into pairs is motivated by the following three arguments, and consequences
 441 on the results will be discussed in § 7.

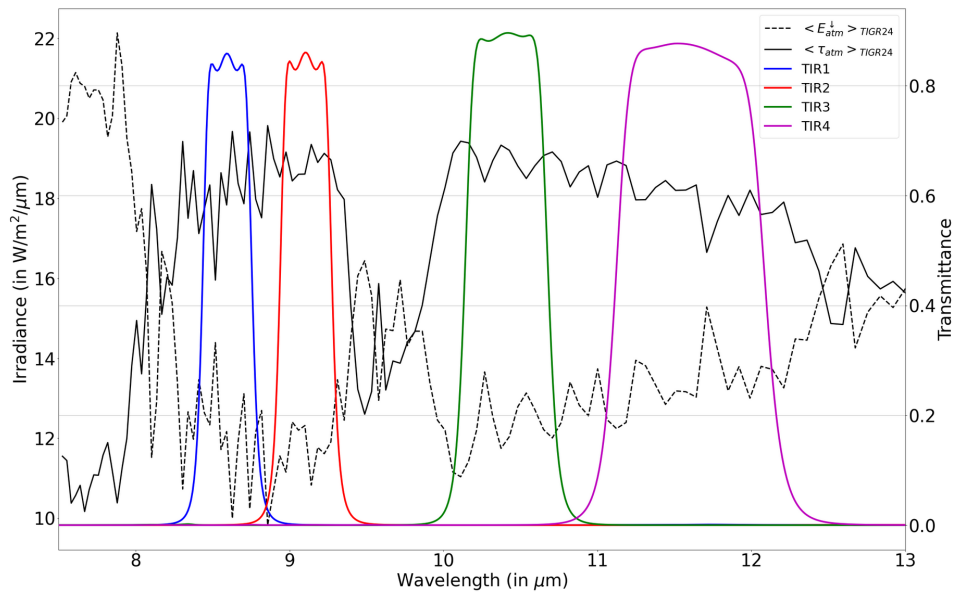


Figure 3: Representation of the TRISHNA reference ISRF for spectral channels TIR1 (blue), TIR2 (red), TIR3 (green) and TIR4 (magenta). The mean atmospheric transmittance and downwelling irradiance over the profiles of the TIR24 dataset, $\langle \tau_{atm} \rangle_{TIGR24}$ and $\langle E_{atm}^\downarrow \rangle_{TIGR24}$, are respectively displayed in black solid and dotted lines.

- 442 1. The TES method is designed to perform best when the spectral configuration captures the spectral variability of the observed scene (§ 1 and 2.1).
 443 According to the subset of natural samples (rocks, soils, vegetation, water and ice) within the ASTER database of emissivity spectra, the average
 444 trend for emissivity variation is typified by minimum values between 8 μm and 9.5 μm , and maximum values between 10 μm and 12 μm (see Figure
 445 7 in Lagouarde et al., 2013). Therefore, the TIR1/TIR2 and TIR3/TIR4
 446 pairs can be studied separately, since they permit to capture the minimum and maximum emissivity values for typical natural targets.
 447
 448
 449
 450
 451 2. This separation is consistent with the TRISHNA mission requirements, which specify that two spectral channels shall be located within the [10 μm -
 452 12 μm] spectral domain for operational application of the SW method.
 453
 454 3. As compared to simultaneous variations of all four TRISHNA channels, studying the TIR1/TIR2 and TIR3/TIR4 pairs separately significantly
 455 reduces the number of channel configurations, and subsequently the computation load.
 456
 457

458 For the TIR1/TIR2 pair study, the variations of position considered are:

- 459 • for λ_c^{TIR1} , from 8 to 9 μm with a step of 0.1 μm ;
- 460 • for λ_c^{TIR2} , from 8.2 to 9.2 μm with a step of 0.1 μm ;

461 In order to keep the same channel order, we set $\lambda_c^{TIR1} \leq \lambda_c^{TIR2}$ with possible
 462 channel superimposition. At the same time, TIR3 and TIR4 are set to their
 463 reference positions, *i.e.*, $\lambda_c^{TIR3} = 10.4 \mu\text{m}$ and $\lambda_c^{TIR4} = 11.6 \mu\text{m}$ respectively
 464 (§ 5.1). This experimental design leads to the generation of 85 ISRFs. When
 465 convolved with the 32,520 TOA radiances described in § 4.3, we obtain $85 \times$
 466 $32,520 = 2,764,200$ OS radiances for our sensitivity study. We note that λ_c^{TIR1}
 467 can slide down to 8 μm , where it crosses the water vapor absorption feature
 468 below 8.25 μm . This permits to highlight the sensitivity of the TES performance
 469 to this absorption feature.

470 For the TIR3/TIR4 pair study, the variations of position considered are:

471 • for λ_c^{TIR3} , from 9.5 to 11 μm with a step of 0.1 μm ;

472 • for λ_c^{TIR4} , from 10.5 to 12 μm with a step of 0.1 μm ;

473 As for the TIR1/TIR2 pair, we set $\lambda_c^{TIR3} \leq \lambda_c^{TIR4}$ with possible channel su-
474 perimposition. At the same time, TIR1 and TIR2 are set to their reference
475 positions, *i.e.*, $\lambda_c^{TIR1} = 8.6 \mu\text{m}$ and $\lambda_c^{TIR2} = 9.1 \mu\text{m}$ respectively (§ 5.1). This
476 experimental design leads to the generation of 241 ISRFs, which results in a total
477 of $241 \times 32,520 = 7,837,320$ OS radiances for our sensitivity study. Similarly to
478 λ_c^{TIR1} in the TIR1/TIR2 case, λ_c^{TIR3} can slide down to 9.5 μm , where it crosses
479 the ozone absorption feature at 9.7 μm . This permits to highlight the sensitivity
480 of the TES performance to this absorption feature. This crossing with the ozone
481 absorption feature is done for TIR3 but not for TIR2, since similar results are
482 expected for both channels. Finally, λ_c^{TIR4} cannot slide above 12 μm , which is
483 justified by a conceptual issue due to the complexity of implementing a detector
484 with such a high cutoff frequency.

485 5.3. Study on the robustness of the reference spectral configuration

486 Instrumental design makes mandatory the consideration of uncertainties on
487 the position and FWHM of each channel. For this purpose, we address the
488 robustness of the TRISHNA reference spectral configuration to these uncertain-
489 ties. The goal is to anticipate how the TES performance would be impacted by
490 such uncertainties, and to evaluate if the observed impacts call for modifications
491 of the spectral configuration. For this, we define realistic uncertainty margins
492 for both the position and FWHM of each spectral channel, respectively labelled
493 $u(\lambda_i)$ and $u(FWHM_i)$, as presented in Table 4. Note that these uncertainty
494 margins are typical of those stated by instrument manufacturers.

495 Considering these uncertainties, we defined four worst-case spectral config-
496 urations with respect to atmospheric perturbations, where each of them corre-
497 sponds to the displacement of one channel from the TRISHNA reference spectral
498 configuration presented in § 5.1.

Table 4: Uncertainties on the position of the central wavelength and on the FWHM of each TRISHNA spectral channel considered in the robustness study.

	TIR1	TIR2	TIR3	TIR4
$u(\lambda_i)$ (μm)	± 0.15	± 0.15	± 0.15	± 0.15
$u(FWHM_i)$ (μm)	± 0.07	± 0.07	± 0.15	± 0.15

- 499 1. A case where TIR1 is fully shifted to lower wavelengths, *i.e.*, consider-
500 ing $\lambda_c^{TIR1} = 8.6 \mu\text{m} - 0.15 \mu\text{m} = 8.45 \mu\text{m}$, with maximum bandwidth
501 $FWHM_{TIR1} = 0.35 \mu\text{m} + 0.07 \mu\text{m} = 0.42 \mu\text{m}$. This corresponds to the
502 case where TIR1 would be most affected by the loss of transmission due
503 to atmospheric water vapor absorption below $8.25 \mu\text{m}$.
- 504 2. A case where TIR2 is fully shifted to larger wavelengths, *i.e.*, consider-
505 ing $\lambda_c^{TIR2} = 9.1 \mu\text{m} + 0.15 \mu\text{m} = 9.25 \mu\text{m}$, with maximum bandwidth
506 $FWHM_{TIR2} = 0.35 \mu\text{m} + 0.07 \mu\text{m} = 0.42 \mu\text{m}$. This corresponds to the
507 case where TIR2 would be most affected by the loss of transmission due
508 to ozone absorption at $9.7 \mu\text{m}$.
- 509 3. A case where TIR3 is fully shifted to lower wavelengths, *i.e.*, consider-
510 ing $\lambda_c^{TIR3} = 10.4 \mu\text{m} - 0.15 \mu\text{m} = 10.25 \mu\text{m}$, with maximum bandwidth
511 $FWHM_{TIR3} = 0.70 \mu\text{m} + 0.15 \mu\text{m} = 0.85 \mu\text{m}$. This corresponds to the
512 case where TIR3 would be most affected by the loss of transmission due
513 to ozone absorption at $9.7 \mu\text{m}$.
- 514 4. A case where TIR4 is fully shifted to larger wavelengths, *i.e.*, considering
515 $\lambda_c^{TIR4} = 11.6 \mu\text{m} + 0.15 \mu\text{m} = 11.75 \mu\text{m}$, with maximum bandwidth
516 $FWHM_{TIR4} = 1.00 \mu\text{m} + 0.15 \mu\text{m} = 1.15 \mu\text{m}$. This corresponds to the
517 case where TIR4 would be most affected by the loss of transmission due
518 to atmospheric water vapor absorption at $12.5 \mu\text{m}$.

519 For each of these 4 worst-case scenarii, we calculated root mean square errors
520 (RMSEs) on TES retrievals of surface temperature, by using the protocol pre-
521 sented in § 4.3 to simulate the dedicated 32,520 TOA radiances.

522 6. Results of the sensitivity analysis

523 We present in this section the results of our sensitivity analysis for both the
524 TIR1/TIR2 and TIR3/TIR4 variation cases. We first detail how the various
525 TES calibrations are conducted, to continue with the results of our sensitivity
526 analysis for both variation cases. Eventually, we present the results we obtained
527 when studying robustness of the TRISHNA reference spectral configuration to
528 uncertainties on channel position and FWHM. In the following, we mostly con-
529 centrate on the results obtained for T_{sur}^{TES} . Indeed, as compared to land surface
530 emissivity, LST is our decision variable, since it is the first order parameter to
531 be used when defining the TRISHNA products.

532 6.1. Calibration of the TES MMD equation

533 For each of the $85 + 241 = 326$ ISRFs used in this study, the coefficients A,
534 B, and C of the ε_{min} -MMD relationship (equation 9) were calibrated over the
535 SAIL271 dataset. The RMSE was calculated, for each spectral configuration,
536 as the calibration residual error.

537 The obtained RMSE values for calibration and validation were all lower than
538 0.008. Table 5 displays averaged values of the coefficients A, B and C for each
539 of the TIR1/TIR2 and TIR3/TIR4 study cases, along with the corresponding
540 coefficients of variation. As observed in previous studies, the MMD calibration
541 values do not vary much from one spectral configuration to another for a given
542 number of channels (Sobrino and Jiménez-Muñoz, 2014; Jacob et al., 2017).
543 As compared to former studies dealing with 4 TIR bands, our coefficients are
544 larger, by 15% and 10% relative, for parameter B and C respectively. Apart
545 from maximum values of ISRF $S_i(\lambda)$, that were lower in our study (0.85 versus
546 0.9), no other explanation could be found for these larger values of parameters
547 B and C.

548 6.2. TIR1/TIR2 case results

549 After performing atmospheric corrections, we computed T_{sur}^{TES} and $(\varepsilon_i^{TES})_{i \in [1; N_B]}$
550 for each of the 2 764 200 OS radiances defined in § 5.2, and we calculated RM-

Table 5: Pairs of (mean value / coefficient of variation) obtained for the calibrated MMD coefficients A, B and C in both TIR1/TIR2 and TIR3/TIR4 study cases.

	A	B	C
TIR1/TIR2 case	0.984 / 0.17%	0.815 / 1.90%	0.912 / 1.80%
TIR3/TIR4 case	0.988 / 0.03%	0.834 / 2.80%	0.926 / 0.10%

SEs for each of the 85 spectral configurations. Figure 4 displays the RMSEs obtained for surface temperature when considering (a) known and (b) noised atmospheric profiles, where known and noised atmospheric profiles correspond to accurate and inaccurate atmospheric corrections, respectively. What directly strikes in Figure 4 is that the TES retrievals of surface temperature are relatively in sensitive to the TIR1 and TIR2 channel positions, with respective maximum RMSE variations of 0.23 K and 0.15 K.

Figure 4(a) shows that for accurate atmospheric corrections (known atmospheric profiles), a large RMSE gradient is observed along the λ_c^{TIR1} axis. In this case, RMSE increases as wavelength decreases, with maximum RMSEs obtained at $\lambda_c^{TIR1} = 8.0 \mu\text{m}$ and a sharp increase from 8.1 to 8.0 μm . Figure 4(b) shows that for inaccurate atmospheric corrections (noised atmospheric profiles), an additional RMSE gradient occurs along the λ_c^{TIR2} axis, although it remains less significant than the one along the λ_c^{TIR1} axis. These RMSEs variations are explained by the TES sensitivity to inaccurate atmospheric corrections (Gillespie et al., 1998; Sobrino and Jiménez-Muñoz, 2014), where this sensitivity is enhanced when both TIR1 and TIR2 channels come closer to the beginning of the water vapor absorption feature at 8.25 μm (decrease in atmospheric transmittance).

Interestingly, bringing the two channels closer seems to have little effect on the surface temperature RMSE, with minimum RMSE values obtained when both channels are centered on wavelengths larger than 8.7 μm .

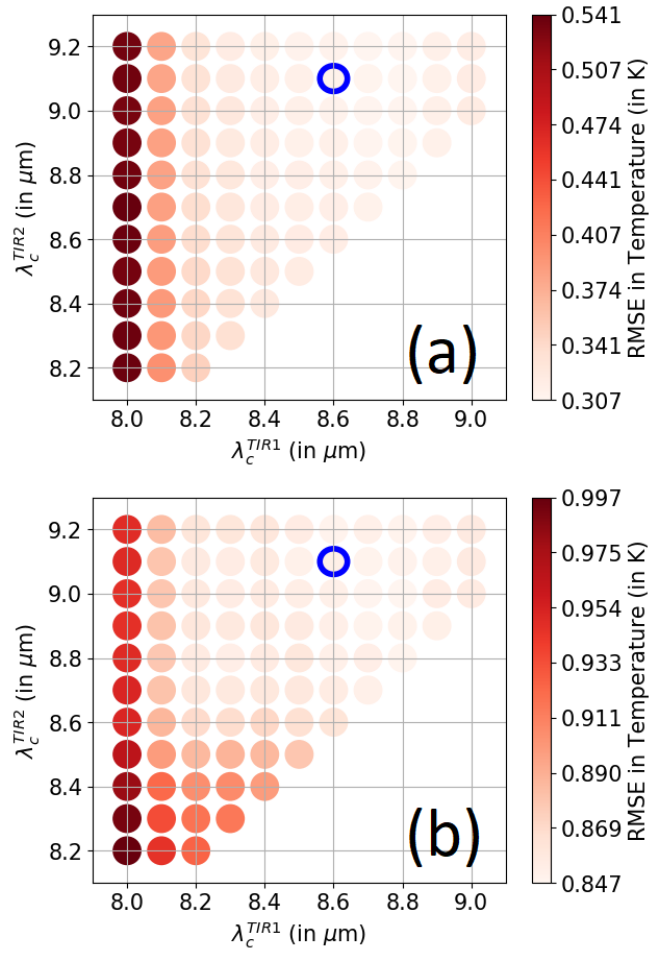


Figure 4: RMSEs in surface temperature obtained in the TIR1/TIR2 study, without (a) and with (b) atmospheric noise. The blue circle highlights in each case the reference spectral configuration: (a) $RMSE(T_{sur}) = 0.31\text{K}$, (b) $RMSE(T_{sur}) = 0.85\text{K}$.

573 *6.3. TIR3/TIR4 case results*

574 Figure 5 is the same as Figure 4 but for the TIR3 and TIR4 positions defined
 575 in § 5.2. When considering accurate atmospheric corrections (Figure 5(a)), and
 576 similarly to the TIR1/TIR2 study case, the TES method is not very sensitive to
 577 the position of the two channels, with a maximum RMSE variation of 0.19 K.
 578 We note two main features from Figure 5(a):

- 579 1. increases in RMSEs are observed towards both limits of the λ_c^{TIR4} interval,
 580 with maximum RMSEs at $\lambda_c^{TIR4} = 10.4 \mu\text{m}$;
- 581 2. a region with local minimum RMSEs is observed for $\lambda_c^{TIR3} \in [9.5\mu\text{m} ;$
 582 $9.6\mu\text{m}]$.

583 On the other hand, a clear increase in RMSEs appears around $9.7 \mu\text{m}$ when
 584 considering inaccurate atmospheric corrections (Figure 5(b)), which clearly indi-
 585 cates a sensitivity of the TES method to ozone and water vapor absorption. This
 586 sensitivity increases the maximum RMSE variation by more than a factor 2, as
 587 compared to the case of accurate atmospheric corrections, namely 0.42 K. Thus,
 588 a maximum RMSE of 1.16 K is obtained for channel locations corresponding to
 589 lower atmospheric transmittance, namely $\lambda_c^{TIR3} = 9.6 \mu\text{m}$ that corresponds to
 590 ozone absorption and $\lambda_c^{TIR4} = 12.0 \mu\text{m}$ that corresponds to water vapor absorp-
 591 tion. For the same reason, an RMSE gradient is observed along the λ_c^{TIR4} axis,
 592 with RMSEs increasing as λ_c^{TIR4} increases, since atmospheric transmittance de-
 593 creases because of water vapor absorption (see Figure 3). When restricting the
 594 TIR3 location between $10.0 \mu\text{m}$ and $11.0 \mu\text{m}$, the sensitivity of the TES method
 595 to TIR3 and TIR4 positions is lowered, with a maximum RMSE variation of
 596 0.305 K. Overall, and conversely to the TIR1/TIR2 case, the sensitivity of the
 597 TES method is increased when considering noise in the TIR3/TIR4 case, which
 598 could be explained by larger atmospheric perturbations on TIR measurements
 599 within the $[11 \mu\text{m} - 12 \mu\text{m}]$ spectral interval, as compared to the $[8.5 \mu\text{m} - 9.5 \mu\text{m}]$
 600 one (see Figure 3).

601 Another result displayed by Figure 5 is that the proximity and even su-
 602 perimposition of the two channels does not significantly deteriorate the TES

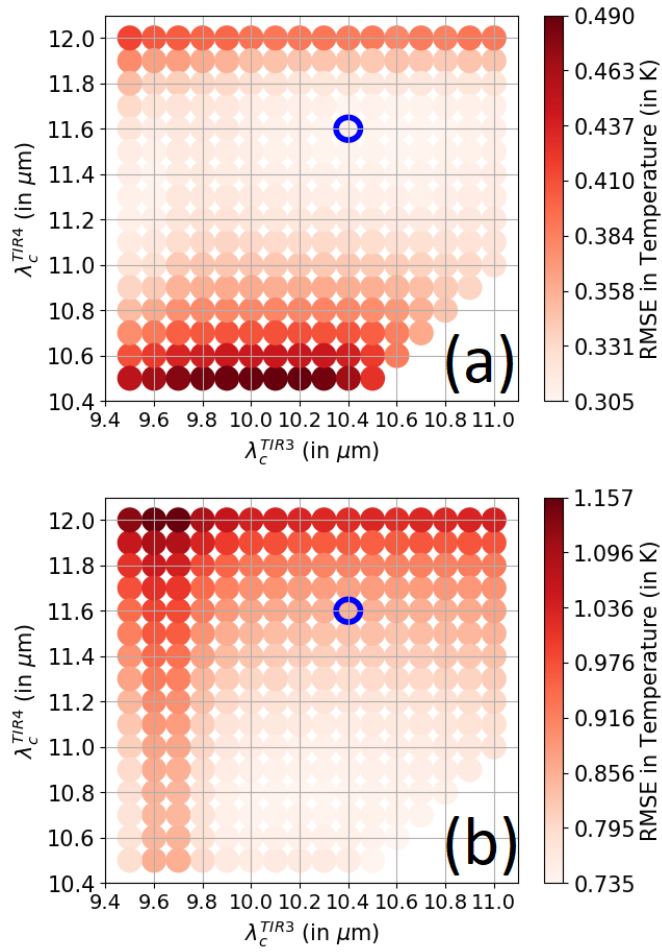


Figure 5: RMSEs in surface temperature obtained in the TIR3/TIR4 study, without (a) and with (b) atmospheric noise. The blue circle highlights in each case the reference spectral configuration: (a) $RMSE(T_{sur}) = 0.31\text{K}$, (b) $RMSE(T_{sur}) = 0.85\text{K}$.

603 performance. This trend, observed for both the TIR1/TIR2 and TIR3/TIR4
 604 cases, suggests that the TES method may have comparable performance when
 605 considering 3 or 4 spectral channels. Its consequence on the design of the TR-
 606 ISHNA instrument, as well as other future similar ones, will be discussed in
 607 § 7.

608 6.4. Results on emissivity

609 The results we obtain for land surface emissivity are similar to those obtained
 610 for land surface temperature. In the case of inaccurate atmospheric corrections,
 611 the sensitivity of the TES method to channel positions is similar for emissivity
 612 and temperature retrievals. Indeed, we observe similar RMSE gradients, espe-
 613 cially for ε_{TIR2}^{TES} and ε_{TIR4}^{TES} (Figure 6 top right versus Figure 4(b) and Figure 6
 614 bottom right versus Figure 5(b)). Furthermore, ε_{TIR2}^{TES} is less sensitive to the de-
 615 crease in λ_c^{TIR1} than ε_{TIR1}^{TES} (Figure 6 top left versus top right), with a difference
 616 in RMSE variations = 0.013. Similarly, ε_{TIR3}^{TES} is less sensitive to the increase in
 617 λ_c^{TIR4} than ε_{TIR4}^{TES} (Figure 6 bottom left versus bottom right). Conversely, the
 618 RMSEs obtained on ε_{TIR4}^{TES} are less impacted by the proximity of λ_c^{TIR3} with
 619 the ozone absorption feature at 9.7 μm , as compared to the RMSEs obtained on
 620 ε_{TIR3}^{TES} . Eventually, these results highlight that the TES retrievals of emissivities
 621 in the case of inaccurate atmospheric corrections behave in the same way as
 622 their temperature counterparts, with a sensitivity that seems directly linked to
 623 the atmospheric transmittance within their respective channels.

624 6.5. Results on the robustness of the spectral configuration

625 For each of the 4 worst-case scenarii for the TRISHNA spectral configuration
 626 related to uncertainties on channel positions and FWHM (§ 5.3), we calculated
 627 RMSEs on TES retrievals of surface temperature. The results, summarized
 628 in Table 6, confirm the overall low sensitivity of the TES method to channel
 629 position and FWHM, even when considering inaccurate atmospheric corrections.
 630 Indeed, the maximum difference with the reference case is 0.07 K, when TIR4
 631 is most affected by water vapor absorption. The results also show that all

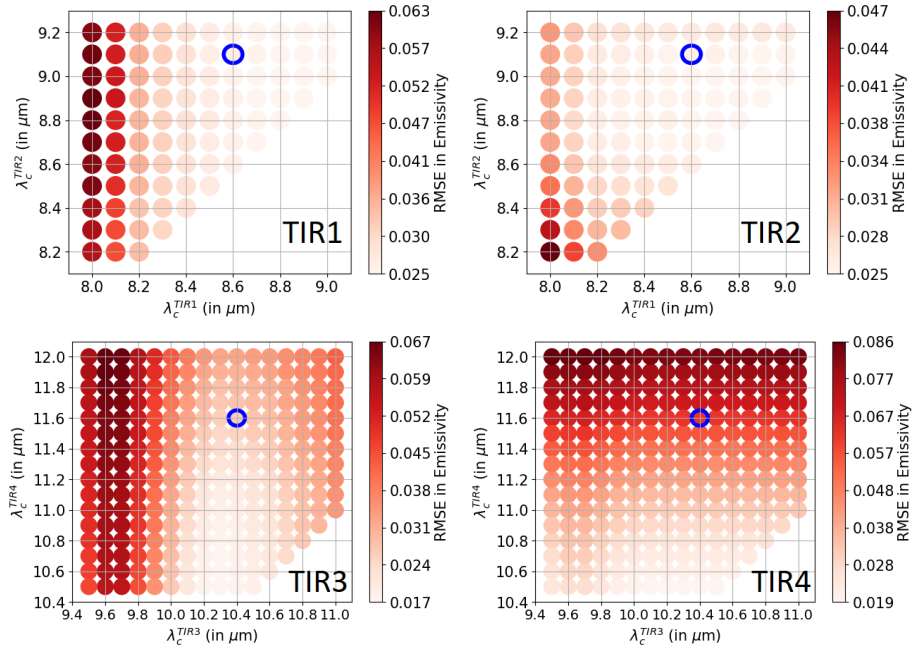


Figure 6: RMSEs in emissivity as obtained in the TIR1/TIR2 study for ε_{TIR1}^{TES} and ε_{TIR2}^{TES} (top panels), and in the TIR3/TIR4 study for ε_{TIR3}^{TES} and ε_{TIR4}^{TES} (bottom panels), all considering atmospheric noise. The blue circle highlights in each case the reference spectral configuration: $RMSE(\varepsilon_{TIR1}^{TES}) = 0.026$, $RMSE(\varepsilon_{TIR2}^{TES}) = 0.025$, $RMSE(\varepsilon_{TIR3}^{TES}) = 0.026$, $RMSE(\varepsilon_{TIR4}^{TES}) = 0.063$.

Table 6: RMSEs on T_{sur}^{TES} obtained in the worst-case scenarii related to uncertainties on channels positions and FWHM defined in § 5.3

Channel (λ_c ,FWHM)	Case	RMSEs on T_{sur}^{TES} (in K)
TIR1 (8.45 μ m,0.42 μ m)	H2O absorption	0.856
TIR2 (9.25 μ m,0.42 μ m)	O ₃ absorption	0.863
TIR3 (10.25 μ m,0.85 μ m)	O ₃ absorption	0.883
TIR4 (11.75 μ m,1.15 μ m)	H2O absorption	0.923
Reference spectral configuration	-	0.850

632 four channels should be located away from their respective nearby absorption
633 feature, in order to maintain low RMSEs (≤ 1 K) when considering worst-cases,
634 and therefore to obtain a TRISHNA spectral configuration that is more robust
635 to uncertainties on channel positions and FWHM.

636 6.6. Recommended TRISHNA spectral configuration

637 The results of the previous section 6.5 permit to define criteria for a possible
638 improvement of the TRISHNA spectral configuration with regards to uncer-
639 tainties on channel positions and FWHM. Despite the apparent equivalence we
640 report for the TES performance between the three and four channels configura-
641 tions, we recommend a four-channels spectral configuration for the TRISHNA
642 mission. This choice is motivated by two main operational arguments, namely
643 (1) to secure the mission continuity in case of channel failures, as encountered
644 with ASTER, LANDSAT and ECOSTRESS, and (2) to allow a better character-
645 ization of land surface emissivity spectra for downstream scientific applications.
646 In this 4-channel configuration, the channel-wise criteria are the following.

- 647 • For TIR1, a shift towards larger wavelengths would attenuate the impact
648 of water vapor absorption below 8.25 μ m. We therefore recommend to
649 slightly shift λ_c^{TIR1} from 8.6 μ m to 8.65 μ m.

- 650 • For TIR2, a shift towards lower wavelengths would mitigate the impact of
651 ozone absorption at 9.7 μm . We therefore recommend to shift λ_c^{TIR2} from
652 9.1 μm to 9.0 μm . Then, the overlap between TIR1 and TIR2 channels
653 would be small, given FWHM values for both channels.
- 654 • For TIR3, a shift towards larger wavelengths would limit the impact of
655 ozone absorption at 9.7 μm . Vidal et al. (2021) reported an optimal posi-
656 tion at 10.6 μm when dealing with the performance of the Split Window
657 method in the context of the TRISHNA mission, and showed that this
658 positioning of TIR3 was robust to the uncertainties on the parameters
659 used in the SW formulations, such as emissivity and AWVC. We therefore
660 recommend to shift λ_c^{TIR3} at 10.6 μm .
- 661 • For TIR4, a shift towards lower wavelengths would attenuate the impact
662 of water vapor absorption above 12 μm . Nonetheless, a limited overlap
663 between TIR3 and TIR4 channel is required to ensure satisfactory per-
664 formance of the Split Window method in the context of the TRISHNA
665 mission (see Vidal et al., 2021). We therefore recommend to keep the
666 original TIR4 position at 11.6 μm .

667 The recommendations listed above lead to the definition of a new TRISHNA
668 spectral configuration, detailed in Table 7 and Figure 7. In order to ensure that
669 this spectral configuration is more robust to uncertainties on channel positions
670 and FWHM than the reference configuration, we compare the corresponding
671 RMSE values on LST to those obtained with the reference spectral configu-
672 ration. For the four worst-case scenarii we consider, apart from TIR4 channel
673 located close to 12 μm , the new configuration slightly improves the performance
674 of the TES inversion, with differences in RMSEs of about 0.02K.

675 The RMSE differences between the two spectral configurations is even lower
676 when comparing the overall TES performance. Indeed, for each case we obtain
677 a RMSE over our 32,520 simulations of 0.850 K and 0.849 K respectively, for a
678 global gain of 0.001 K with the recommended configuration. This apparent low

Table 7: Central wavelength λ_c and FWHM for the TRISHNA recommended channels.

	TIR1	TIR2	TIR3	TIR4
λ_c (μm)	8.65 ± 0.10	9.0 ± 0.10	10.6 ± 0.15	11.6 ± 0.15
FWHM (μm)	0.35 ± 0.07	0.35 ± 0.07	0.7 ± 0.15	1.0 ± 0.15

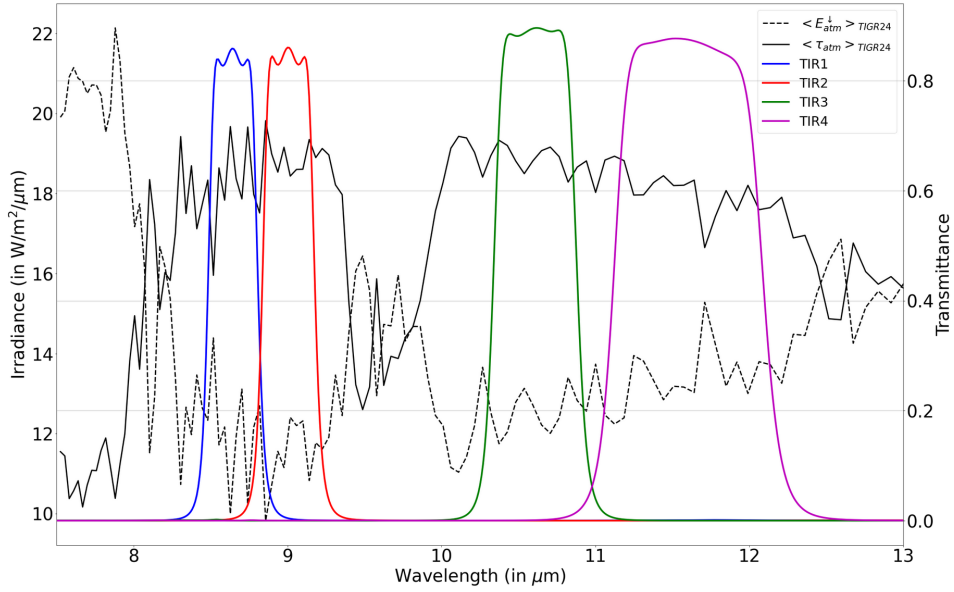


Figure 7: Representation of the TRISHNA recommended ISRF with spectral channels TIR1 (blue), TIR2 (red), TIR3 (green) and TIR4 (magenta). The mean atmospheric transmittance and downwelling irradiance over the profiles of the TIR24 dataset, $\langle \tau_{atm} \rangle_{TIGR24}$ and $\langle E_{atm}^\downarrow \rangle_{TIGR24}$, are respectively displayed in black solid and dotted lines.

679 gain achieved by the spectral channel positions optimization will be discussed
680 in § 7.

681 7. Discussion

682 7.1. On the selection of atmospheric profiles

683 In § 4.2, we detail the TIGR24 subset of atmospheric profiles selected for
684 our study, and highlight that this subset does not conserve the initial profile
685 density of the TIGR dataset in the $T_{atm}^{eq}/AWVC$ plane. Indeed, the comparison
686 between Figure 2(a) and 2(b) shows that the TIGR24 subset drastically reduces
687 the density of dry atmosphere profiles ($AWVC < 2.5 \text{ g.cm}^{-2}$) as compared to
688 the original TIGR dataset. As such, the TIGR24 subset includes fewer dry
689 atmosphere profiles (11) than wet atmosphere profiles (13). However, the cur-
690 rent study is conducted in the context of the TRISHNA mission, which regions
691 of interest include tropical regions such as India. Therefore, it makes sense to
692 assess the TES performance by weighting the occurrence of wet atmospheres.
693 First, atmospheric corrections are less accurate with such wet atmosphere pro-
694 files. Second, accuracy on atmospheric corrections is a first order driver for the
695 performance of the TES method (Gillespie et al., 1998; Jacob et al., 2004, 2017;
696 Schmugge et al., 1998, 2002; Sobrino and Jiménez-Muñoz, 2014). Therefore,
697 accounting for such wet atmosphere profiles to analyze TES performance is rel-
698 evant for the preparation of the TRISHNA mission. Indeed, it is expected that
699 considering more dry atmospheres than in the 'TIGR24' dataset would reduce
700 the RMSEs and result in better TES performance, while mitigating the impact
701 of the more problematic wet atmospheres. In order to provide a realistic evalu-
702 ation of the TES performance in the context of the TRISHNA mission, it would
703 be valuable to quantify the occurrence of dry and wet atmospheric profiles on a
704 global scale. Such a study should be conducted in the context of this mission.

705 7.2. On the TIR1/TIR2 and TIR3/TIR4 pairs separation

706 It is explained in § 5.2 that our sensitivity study is based on sliding the
707 positions of two TRISHNA channels at the same time, by considering separately

708 the TIR1/TIR2 and TIR3/TIR4 pairs of channels. As opposed to moving the
709 positions of all four channels at the same time, this trade-off is motivated by
710 the considerations discussed below.

- 711 1. For the use of the TES method, these two pairs of channels have distinct
712 tasks, namely capturing the minimum (for TIR1/TIR2) and maximum
713 (for TIR3/TIR4) emissivity values across the emissivity spectra of natural
714 targets. In order to do so, we locate these pairs within spectral intervals
715 for which atmospheric and emissivity-related properties are known to be
716 optimal for TES application, namely $[8 \mu\text{m} - 9.5 \mu\text{m}]$ and $[10 \mu\text{m} - 12 \mu\text{m}]$,
717 respectively (Lagouarde et al., 2013). Therefore, sliding in pairs permits
718 to study the positioning of channels in the context of their respective roles
719 in these spectral intervals.
- 720 2. The consideration of four sliding channels would result in a number of
721 simulations that would exceed our computational capability. Indeed, even
722 considering a reduced interval for TIR3 outside of atmospheric ozone ab-
723 sorption between $10 \mu\text{m}$ and $11 \mu\text{m}$ would increase the number of simula-
724 tions by a factor 50, for over 500 millions of simulations in that case.

725 Given the operational aspect of the TRISHNA mission, the conclusions
726 drawn in this study are based on the results obtained in the operational case
727 (inaccurate atmospheric corrections). In that case, the factors that can affect
728 the TES performance are supposedly (1) the instrumental noise, (2) inaccurate
729 atmospheric corrections, and (3) variation of the observed emissivity which con-
730 trast has to be correctly measured for the TES method. On the one hand, we
731 do not observe any sensitivity to the instrumental noise in the operational case.
732 Moreover, we run for the sake of completeness the TIR1/TIR2 and TIR3/TIR4
733 cases with inaccurate atmospheric corrections but no instrumental noise. The
734 results obtained show similar RMSE variations than in the operational case
735 (Figure 4(b) and 5(b)), and the RMSE differences between both cases are of an
736 order of magnitude of a few 10^{-3} K. This suggests that TES is faintly sensitive
737 to instrumental noise in the operational case. On the other hand, results of

738 § 6.2 and 6.3 show a moderate sensitivity of TES to channel positions, which
739 appears to be due to variations of atmospheric perturbations in the operational
740 case, notably in the case of the TIR1/TIR2 pair. Indeed, this case was expected
741 to result in a higher TES sensitivity to channel position than the TIR3/TIR4,
742 given the variation of emissivity observed in the $[8 \mu\text{m} - 9.5 \mu\text{m}]$ spectral interval
743 as compared to the $[10 \mu\text{m} - 12 \mu\text{m}]$ interval (Lagouarde et al., 2013). This re-
744 sult supports the hypothesis that in the operational case, the TES performance
745 depends mainly on atmospheric perturbations rather than emissivity variations.
746 This main dependency to atmospheric conditions, which implies that the TES
747 sensitivity to channel positions within atmospheric windows is moderate, hints
748 that sliding at the same time the four TRISHNA TIR channels is likely to
749 provide similar results on TES performance as obtained in this study, as well
750 as similar recommendations for an optimized TRISHNA spectral configuration,
751 provided that TRISHNA channels are not located nearby the limits of the at-
752 mospheric window. This statement is also supported by the similarity between
753 the results of the current study and those reported for the MISTIGRI mission
754 (Jacob et al., 2021) with different spectral configurations including more than
755 two channels.

756 *7.3. On the TES performance with known atmospheres*

757 On the one hand, result analysis in § 6.2 and 6.3, including interpretation
758 of Figures 4(b) and 5(b), underline the sensitivity of the TES method to atmo-
759 spheric perturbations related to water vapor absorption (TIR1, TIR2 and TIR4)
760 and ozone absorption (TIR3). This is consistent with former studies that re-
761 ported similar sensitivities (Gillespie et al., 1998; Jacob et al., 2004; Schmugge
762 et al., 1998, 2002; Sobrino and Jiménez-Muñoz, 2014).

763 On the other hand, Figures 4(a) and 5(a) indicate a large sensitivity of
764 the TES method to the TIR1 and TIR4 channel positions when considering
765 accurate atmospheric corrections. For the TIR1/TIR2 case, RMSE values on
766 TES retrievals of surface temperature increase as TIR1 slides toward $8.0 \mu\text{m}$. For
767 the TIR3/TIR4 case, RMSE values increase when TIR4 comes closer to either

768 10.5 μm or 12 μm , which induces a region with lower RMSE values between
 769 both limits. Additionally, the TES sensitivity to TIR3 channel position relative
 770 to ozone absorption at 9.7 μm is very low. Considering the underlying physical
 771 processes at play, possible explanations involve the impact of both atmospheric
 772 downwelling irradiance and instrumental noise.

- 773 1. Jacob et al. (2017) reported a large sensitivity of the TES method to
 774 the atmospheric downwelling irradiance below 8.5 μm . This is consistent
 775 with the gradient of RMSE values along the TIR1 axis in Figure 4(a),
 776 and in accordance with the change of atmospheric downwelling irradiance
 777 within this spectral domain due to water vapor absorption (Figures 3
 778 and 7). The same physical process, namely water vapor absorption, also
 779 explains the increase of RMSE values when TIR4 comes closer to 12.0 μm
 780 in Figure 5(a). Overall, the impact of atmospheric downwelling irradiance
 781 can be explained by Equation 11, where any error on emissivity retrieval
 782 is enhanced by the weighting of atmospheric downwelling irradiance.
- 783 2. In case of accurate atmospheric corrections, a possible perturbation of TES
 784 performance is the instrumental noise. In the current study, the latter is
 785 expressed as a white noise that accounts for dark current and quantifi-
 786 cation (§ 3.3.2). Figure 8 displays the quadratic value of $\text{Ne}\Delta\text{L}$ obtained
 787 with the PERSEUS instrument module for the TIR3 (left panel) and TIR4
 788 (right panel) channels, in the TIR3/TIR4 study case. On the one hand,
 789 a clear RMS gradient along the λ_c^{TIR3} axis is observed in the $\text{Ne}\Delta\text{L}_{\text{TIR3}}$
 790 case, with RMS decreasing as wavelength decreases down to 9.6 μm near
 791 the ozone atmospheric feature. On the other hand, an RMS gradient is
 792 observed along the λ_c^{TIR4} axis for the $\text{Ne}\Delta\text{L}_{\text{TIR4}}$ case, with RMS increas-
 793 ing as wavelength decreases. The combination of both quadratic noises
 794 $\text{Ne}\Delta\text{L}_{\text{TIR3}}$ and $\text{Ne}\Delta\text{L}_{\text{TIR4}}$ can explain the RMSE variations observed in
 795 Figure 5(a) for TES retrievals of surface temperature. More particularly,
 796 it can explain the lowest RMSE values obtained across the ozone atmo-
 797 spheric feature at 9.7 μm , and the largest RMSE values obtained when

798 λ_c^{TIR4} decreases down to $10.5 \mu\text{m}$. Eventually, these results are confirmed
799 by the fact that the magnitude of the $\text{Ne}\Delta\text{L}$ variations observed in Figure 8
800 corresponds to the magnitude of their corresponding surface temperature
801 RMSE variations in Figure 5(a), where both magnitudes are compared
802 using Planck's law (Equation 6).

803 The aforementioned considerations also suggest that the TES method is more
804 sensitive to instrumental noise than to uncertainties on atmospheric downwelling
805 irradiance, when used without atmospheric perturbations. Indeed, the lowest
806 RMSE values for surface temperature in Figure 5(a) are obtained across the
807 ozone emission feature centered at $9.7 \mu\text{m}$. However, further investigations on
808 the sensitivity of the TES method to the combination of these two driving factors
809 are needed to conclude on this issue.

810 For sake of completeness, we also address in Figure 9 the variations of calibra-
811 tion RMSEs for the $\varepsilon_{min} - \text{MMD}$ relationship (Equation 9). The obtaining of
812 these calibration RMSE values for both TIR1/TIR2 and TIR3/TIR4 study cases
813 are described in § 6.1. Both Figure 9(a) and (b) display a low sensitivity of the
814 MMD calibration to the channel positions, with maximum RMSE variations of
815 0.0007 and 0.0021 for the TIR1/TIR2 and TIR3/TIR4 case study, respectively.
816 These low variations cannot explain the surface temperature RMSE variations
817 of 0.233 K and 0.185 K observed in Figure 4(a) and 5(a), respectively. Moreover,
818 we observe different patterns in Figure 9(a) and (b), as compared to those dis-
819 played in Figure 4(a) and 5(a), except for the increase in RMSE with decreasing
820 λ_c^{TIR4} in Figure 9(b). However, as mentioned above, this decrease in Figure 5(a)
821 is likely to be due to instrumental noise, notably given the low magnitude of
822 the calibration RMSE values. These results support the idea that with accurate
823 atmospheric corrections, TES is primarily sensitive to instrumental noise and
824 atmospheric downwelling irradiance.

825 7.4. On the TES performance with 3 or 4 channels

826 The results presented in this paper hint at the fact that when superimposing
827 two of the four spectral channels considered, the TES performance does not

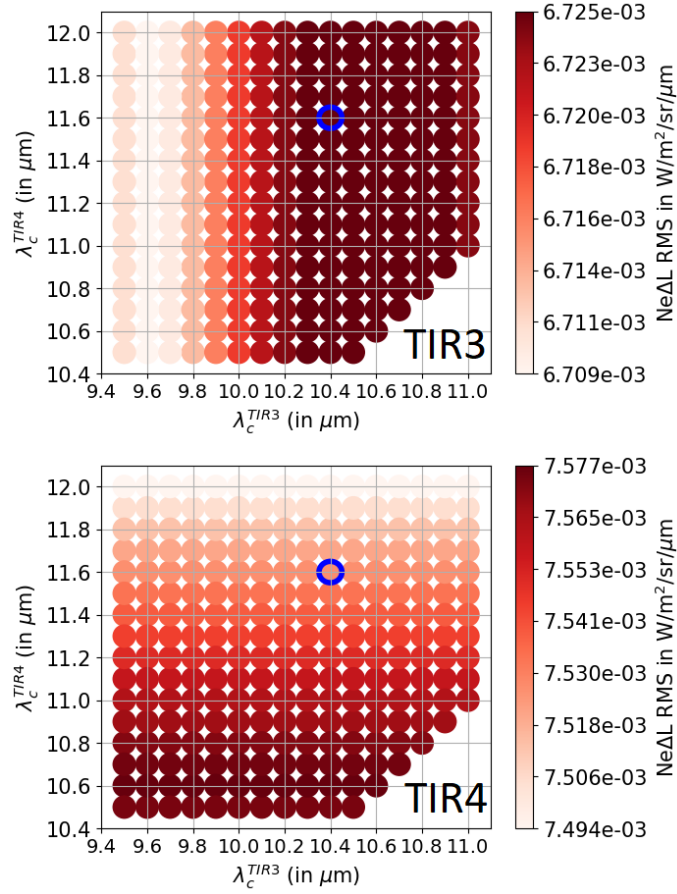


Figure 8: Quadratic values (labelled RMS for Root mean square) of $\text{Ne}\Delta\text{L}$ obtained from the instrument module when considering the TIR3 (left panel) and TIR4 (right panel) channels. The blue circle highlights in each case the reference spectral configuration: $\text{RMS}(\text{Ne}\Delta\text{L}_{\text{TIR3}}) = 6.725 \times 10^{-3} \text{ W}\cdot\text{m}^{-2}\cdot\text{sr}^{-1}\cdot\mu\text{m}^{-1}$ and $\text{RMS}(\text{Ne}\Delta\text{L}_{\text{TIR4}}) = 7.526 \times 10^{-3} \text{ W}\cdot\text{m}^{-2}\cdot\text{sr}^{-1}\cdot\mu\text{m}^{-1}$.

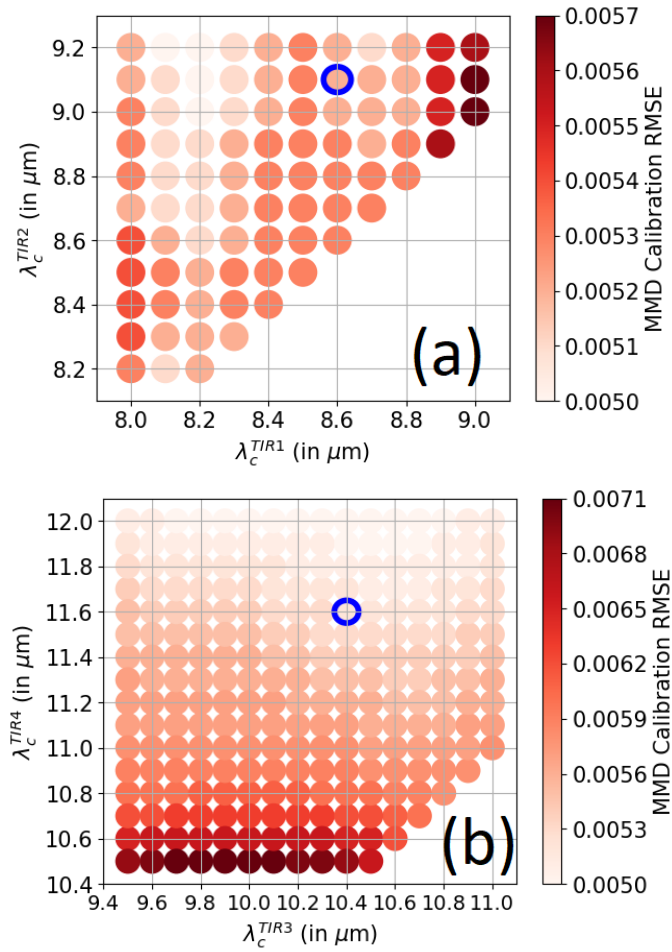


Figure 9: Calibration RMSEs of the MMD equation (9) as computed in the TIR1/TIR2 case (a), and in the TIR3/TIR4 case (b). The blue circle highlights in each case the reference spectral configuration with a calibration RMSE of 0.0052.

828 drastically change as compared to other effective spectral configurations. This
829 could reveal that the TES method has similar performance when considering 3 or
830 4 spectral channels. This observation is reinforced by results of previous studies
831 that obtained similar, and sometimes even slightly better, TES performance
832 with three-channels configurations than four-channels ones (Hulley et al., 2010;
833 Sobrino and Jiménez-Muñoz, 2014; Jiménez-Muñoz et al., 2014; Jacob et al.,
834 2017, 2021).

835 From a general point of view, this issue is paramount since a 3-channels con-
836 figuration could sensibly reduce the production cost for any TIR instrument as
837 compared to a 4-channels configuration. A study specifically dedicated to com-
838 pare the performance of these configurations should be conducted in the context
839 of future missions. However, in the context of the TRISHNA mission, as the
840 aforementioned results do not specifically favor the 3 or 4 channels configurations
841 in term of TES performances, we recommend a 4-channels configuration for two
842 main operational reasons, namely (1) to secure the mission continuity in case of
843 channel failures, as encountered with ASTER, LANDSAT and ECOSTRESS,
844 and (2) to allow a better characterization of land surface emissivity spectra for
845 downstream scientific applications.

846 *7.5. On the improvements of the recommended TRISHNA spectral configuration*

847 As compared to the reference TRISHNA spectral configuration, we showed
848 in § 6.6 that the gain on TES performance with the recommended configuration
849 is not significant (≈ 0.001 K). On the one hand, this result can be explained
850 by the overall low sensitivity of TES to channel positions observed in § 6.2
851 and 6.3, especially when considering channels within the atmospheric window.
852 On the other hand, and as reported by Vidal et al. (2021), the performance
853 of the Split Window method is improved with the recommended configuration,
854 showing an overall gain in RMSE of 0.2 K as compared to the reference config-
855 uration. Moreover in the SW case, this configuration is shown to be robust to
856 uncertainties on emissivity, AWVC, and channel positioning. Therefore, even if
857 our recommended spectral configuration does not significantly improve the TES

858 performance for the retrieval of land surface temperature, it improves the per-
859 formance of the Split Window method, while being more robust to uncertainties
860 on channel position and FWHM.

861 *7.6. On the future optimization of the TES method for TRISHNA applications*

862 Although the objective of this study was to evaluate the sensitivity of the
863 TES method to the TRISHNA spectral configuration, the TES method was
864 not numerically optimized for the TRISHNA instrument. We expect that such
865 an optimization would increase the observed performance, therefore improving
866 the quality of the TRISHNA LST and land surface emissivity (LSE) retrievals.
867 Indeed, the several thresholds used in the NEM module (§ 2.1.1) were set in
868 the current study to their ASTER mission values, due to a lack of information
869 for other sensors. On the one hand, considering that both the convergence and
870 divergence thresholds (respectively t_2 and t_1) are supposed to be fixed at the
871 corresponding instrument $Ne\Delta L$ value, and given the fact that the TRISHNA
872 $Ne\Delta L$ value is an order of magnitude lower than the ASTER one, the TES
873 surface temperature estimation is expected to be improved. On the other hand,
874 the remaining thresholds for emissivity refinement could as well be improved
875 using more comprehensive emissivity databases than the ones used to set their
876 ASTER value. This update of the thresholds is also believed to possibly improve
877 the TES estimation of surface temperature and emissivity, especially regarding
878 the distinction between reflective and grey-body materials.

879 **8. Conclusion**

880 From a process perspective, the current study evaluates the sensitivity of
881 the TES method to channel positions and bandwidths in the context of the TR-
882 ISHNA mission with a four-channel configuration. We highlight the sensitivity
883 of the TES method to atmospheric downwelling irradiance and instrumental
884 noise, under conditions of accurate atmospheric corrections. In the case of
885 inaccurate atmospheric corrections, the TES methods is sensitive to channel

886 locations and bandwidths, more particularly when filter response functions ex-
887 tend over spectral intervals with atmospheric perturbations, namely absorption
888 by water vapor and ozone. These results are strengthened by the two following
889 considerations.

- 890 1. On the one hand, the TES method presents a low sensitivity to channel
891 positions within both $[8.25 \mu\text{m} - 9.5 \mu\text{m}]$ and $[10 \mu\text{m} - 12 \mu\text{m}]$ atmospheric
892 windows. On the other hand, the TES performance is slightly degraded
893 when locating channels on spectral interval with atmospheric perturba-
894 tions. Therefore, it does not seem necessary to investigate a finer spectral
895 sampling.
- 896 2. Our results are similar to those reported for the MISTIGRI mission with
897 spectral configurations that differ from the TRISHNA reference (Jacob
898 et al., 2021). Therefore, scanning the spectral space for each of the four
899 channel is likely to provide similar results than scanning the spectral space
900 using separated pairs of channels.

901 From an operational viewpoint, the results of the current study do not con-
902 tradict those reported by Vidal et al. (2021) who addressed the sensitivity of
903 the Split Window method to channel positions and bandwidths in the context
904 of the TRISHNA mission. Overall, both studies converge toward a unique rec-
905 ommendation for the spectral configuration of the TRISHNA mission, with an
906 overall error on surface temperature retrievals of 0.85 K. This is satisfactory in
907 term of mission requirements (≤ 1.5 K), and is of the same order of magnitude
908 as the precision requirements for further applications (0.8 K, cf Seguin et al.,
909 1999; Hernandez-Baquero, 2000).

910 Finally, the precision of the TES method in the context of the TRISHNA
911 mission is likely to be improved in the near future thanks to forthcoming studies,
912 as discussed below.

- 913 1. The prior use of the water vapor scaling method (WVS method, Tonooka,
914 2005) before atmospheric corrections is expected to considerably reduce
915 the RMSE values on TES retrievals of surface temperatures, especially

916 for wet atmospheric conditions ($AWVC \geq 2.5 \text{ g.cm}^{-2}$). Indeed, Tonooka
917 (2005) reported that the expected RMSE on TES LST retrievals is about
918 0.6 K when using the WVS method. This is sensibly lower than the
919 RMSE we obtain in the current study for inaccurate atmospheric correc-
920 tions (0.85 K), as well as twice lower than the mission requirement (1.5 K).

921 2. Research should be conducted on how the TES method could be strength-
922 ened by integrating *a priori* visible and shortwave infrared data, as for
923 instance a first estimate on the emissivity of the considered scene. As
924 mentioned in § 2.1, recent research has shown that such an enhancement
925 could increase the accuracy on TES retrievals for dry atmospheres (Zheng
926 et al., 2019). However, such improvements need to be carefully imple-
927 mented, since it could introduce spatial discontinuities in the temperature
928 retrievals, for instance between vegetated and arid area, as observed with
929 the original TES threshold classifier (Gustafson et al., 2006).

930 From a methodological perspective, we propose an optimization method
931 based on the sliding of channels within respective spectral ranges. This method
932 allows the finding of minimum values of RMSEs in surface temperature and
933 emissivity, within the space defined by the aforementioned spectral ranges. Pro-
934 vided adequate computational capabilities are available, it can be used as such
935 for future multispectral and hyperspectral sensors to find optimal channel posi-
936 tions with respect to any inversion method, either within a given spectral domain
937 among solar and thermal infrared ones, or across both simultaneously. Indeed,
938 due to computational limitations in the current study, we consider the sliding
939 of TRISHNA channels on a pair-basis rather than considering the simultaneous
940 sliding of all four channels. We expect that future improvements of computa-
941 tional capacities will allow more comprehensive studies, such as conducted by
942 Vidal et al. (2021) for the SW channels of the TRISHNA instrument.

943 **Acknowledgment**

944 This work was supported by the French Space Agency (CNES, contract
945 181154) in the context of the preparation of the TRISHNA mission.

946 **References**

947 Barsi, J.A., Barker, J.L., Schott, J.R., 2003. An atmospheric correction parame-
948 ter calculator for a single thermal band earth-sensing instrument, in: IGARSS
949 2003. 2003 IEEE International Geoscience and Remote Sensing Symposium.
950 Proceedings (IEEE Cat. No. 03CH37477), IEEE. pp. 3014–3016.

951 Bayat, B., van der Tol, C., Verhoef, W., 2018. Integrating satellite optical
952 and thermal infrared observations for improving daily ecosystem functioning
953 estimations during a drought episode. *Remote sensing of environment* 209,
954 375–394.

955 Berk, A., Anderson, G.P., 2008. Impact of modtran® 5.1 on atmospheric
956 compensation, in: IGARSS 2008-2008 IEEE International Geoscience and
957 Remote Sensing Symposium, IEEE. pp. III–127.

958 Bigeard, G., Coudert, B., Chirouze, J., Er-Raki, S., Boulet, G., Ceschia, E.,
959 Jarlan, L., 2019. Ability of a soil–vegetation–atmosphere transfer model and
960 a two-source energy balance model to predict evapotranspiration for several
961 crops and climate conditions. *Hydrology and Earth System Sciences* 23, 5033–
962 5058.

963 Cao, B., Guo, M., Fan, W., Xu, X., Peng, J., Ren, H., Du, Y., Li, H., Bian,
964 Z., Hu, T., et al., 2018. A new directional canopy emissivity model based on
965 spectral invariants. *IEEE Transactions on Geoscience and Remote Sensing*
966 56, 6911–6926.

967 Carlson, T.N., Petropoulos, G.P., 2019. A new method for estimating of evapo-
968 transpiration and surface soil moisture from optical and thermal infrared mea-

- 969 surements: The simplified triangle. *International Journal of Remote Sensing*
970 40, 7716–7729.
- 971 Caselles, V., Rubio, E., Coll, C., Valor, E., 1998. Thermal band selection for
972 the prism instrument: 3. optimal band configurations. *Journal of Geophysical*
973 *Research: Atmospheres* 103, 17057–17067.
- 974 Chevallier, F., Chédin, A., Chéruy, F., Morcrette, J.J., 2000. Tigr-like
975 atmospheric-profile databases for accurate radiative-flux computation. *Quar-*
976 *terly Journal of the Royal Meteorological Society* 126, 777–785.
- 977 Coll, C., Caselles, V., Valor, E., Niclòs, R., Sánchez, J.M., Galve, J.M., Mira,
978 M., 2007. Temperature and emissivity separation from aster data for low
979 spectral contrast surfaces. *Remote sensing of environment* 110, 162–175.
- 980 Coll, C., Caselles, V., Valor, E., Rubio, E., 2003. Validation of temperature-
981 emissivity separation and split-window methods from tims data and ground
982 measurements. *Remote Sensing of Environment* 85, 232–242.
- 983 Courault, D., Jacob, F., Benoit, V., Weiss, M., Marloie, O., Hanocq, J.F., Fillol,
984 E., Oliosio, A., Dedieu, G., Gouaux, P., et al., 2009. Influence of agricultural
985 practices on micrometeorological spatial variations at local and regional scales.
986 *International Journal of Remote Sensing* 30, 1183–1205.
- 987 Dash, P., Göttsche, F.M., Olesen, F.S., Fischer, H., 2002. Land surface tem-
988 perature and emissivity estimation from passive sensor data: Theory and
989 practice-current trends. *International Journal of remote sensing* 23, 2563–
990 2594.
- 991 French, A., Schmugge, T., Ritchie, J., Hsu, A., Jacob, F., Ogawa, K., 2008.
992 Detecting land cover change at the jornada experimental range, new mexico
993 with aster emissivities. *Remote Sensing of Environment* 112, 1730–1748.
- 994 French, A.N., Jacob, F., Anderson, M.C., Kustas, W.P., Timmermans, W.,
995 Gieske, A., Su, Z., Su, H., McCabe, M.F., Li, F., et al., 2005. Surface energy

996 fluxes with the advanced spaceborne thermal emission and reflection radiome-
997 ter (aster) at the iowa 2002 smacex site (usa). *Remote sensing of environment*
998 *99*, 55–65.

999 Galleguillos, M., Jacob, F., Prévot, L., French, A., Lagacherie, P., 2011. Com-
1000 parison of two temperature differencing methods to estimate daily evapotran-
1001 spiration over a mediterranean vineyard watershed from aster data. *Remote*
1002 *Sensing of Environment 115*, 1326–1340.

1003 Galleguillos, M., Jacob, F., Prévot, L., Lagacherie, P., Liang, S., 2010. Mapping
1004 daily evapotranspiration over a mediterranean vineyard watershed. *IEEE*
1005 *Geoscience and Remote Sensing Letters 8*, 168–172.

1006 Gillespie, A., Rokugawa, S., Matsunaga, T., Cothorn, J.S., Hook, S., Kahle,
1007 A.B., 1998. A temperature and emissivity separation algorithm for advanced
1008 spaceborne thermal emission and reflection radiometer (aster) images. *IEEE*
1009 *Transactions on Geoscience And Remote Sensing 36*, 1113–1126.

1010 Gillespie, A.R., Rokugawa, S., Hook, S.J., Matsunaga, T., Kahle, A.B., 1999.
1011 Temperature/emissivity separation algorithm theoretical basis document, ver-
1012 sion 2.4. ATBD contract NAS5-31372, NASA .

1013 Girouard, G., Bannari, A., El Harti, A., Desrochers, A., 2004. Validated spectral
1014 angle mapper algorithm for geological mapping: comparative study between
1015 quickbird and landsat-tm, in: XXth ISPRS congress, geo-imagery bridging
1016 continents, Istanbul, Turkey, pp. 12–23.

1017 Gómez, M., Oliso, A., Sobrino, J., Jacob, F., 2005. Retrieval of evapotranspi-
1018 ration over the alpillles/reseda experimental site using airborne polder sensor
1019 and a thermal camera. *Remote Sensing of Environment 96*, 399–408.

1020 Göttsche, F.M., Hulley, G.C., 2012. Validation of six satellite-retrieved land
1021 surface emissivity products over two land cover types in a hyper-arid region.
1022 *Remote Sensing of Environment 124*, 149–158.

- 1023 Grigsby, S.P., Hulley, G.C., Roberts, D.A., Scheele, C., Ustin, S.L., Alsina,
1024 M.M., 2015. Improved surface temperature estimates with master/aviris sen-
1025 sor fusion. *Remote Sensing of Environment* 167, 53–63.
- 1026 Guillevic, P., Gastellu-Etchegorry, J., Demarty, J., Prévot, L., 2003. Thermal
1027 infrared radiative transfer within three-dimensional vegetation covers. *Journal*
1028 *of Geophysical Research: Atmospheres* 108.
- 1029 Gustafson, W.T., Gillespie, A.R., Yamada, G.J., 2006. Revisions to the aster
1030 temperature/emissivity separation algorithm, in: 2nd International Sympo-
1031 sium on Recent Advances in Quantitative Remote Sensing, Global Change
1032 Unit, University of Valencia Torrent, Spain. pp. –.
- 1033 Hernandez-Baquero, E.D., 2000. Characterization of the Earth’s surface and
1034 atmosphere from multispectral and hyperspectral thermal imagery. Technical
1035 Report. Air Force Institute of Technology Wright-Patterson, AFB OH, School
1036 Of Engineering.
- 1037 Hulley, G., Hook, S., Baldrige, A., 2008. Aster land surface emissivity database
1038 of california and nevada. *Geophysical Research Letters* 35.
- 1039 Hulley, G., Hook, S., Fisher, J., Lee, C., 2017. Ecostress, a nasa earth-ventures
1040 instrument for studying links between the water cycle and plant health over
1041 the diurnal cycle, in: IGARSS 2017-2017 IEEE International Geoscience and
1042 Remote Sensing Symposium, IEEE. pp. 5494–5496.
- 1043 Hulley, G.C., Hook, S.J., 2010. Generating consistent land surface temperature
1044 and emissivity products between aster and modis data for earth science re-
1045 search. *IEEE Transactions on Geoscience and Remote Sensing* 49, 1304–1315.
- 1046 Hulley, G.C., Hook, S.J., Baldrige, A.M., 2010. Investigating the effects of
1047 soil moisture on thermal infrared land surface temperature and emissivity
1048 using satellite retrievals and laboratory measurements. *Remote Sensing of*
1049 *Environment* 114, 1480–1493.

- 1050 Hulley, G.C., Hughes, C.G., Hook, S.J., 2012. Quantifying uncertainties in land
1051 surface temperature and emissivity retrievals from aster and modis thermal
1052 infrared data. *Journal of Geophysical Research: Atmospheres* 117.
- 1053 Inoue, Y., Oliosio, A., Choi, W., 2004. Dynamic change of co2 flux over bare
1054 soil field and its relationship with remotely sensed surface temperature. *In-*
1055 *ternational Journal of Remote Sensing* 25, 1881–1892.
- 1056 Jacob, F., Gu, X., Hanocq, J.F., Tallet, N., Baret, F., 2003. Atmospheric
1057 corrections of single broadband channel and multidirectional airborne thermal
1058 infrared data: application to the reseda experiment. *International Journal of*
1059 *Remote Sensing* 24, 3269–3290.
- 1060 Jacob, F., Lesaignoux, A., Oliosio, A., Weiss, M., Caillaud, K., Jacquemoud, S.,
1061 Nerry, F., French, A., Schmugge, T., Briottet, X., et al., 2017. Reassessment
1062 of the temperature-emissivity separation from multispectral thermal infrared
1063 data: Introducing the impact of vegetation canopy by simulating the cavity
1064 effect with the sail-thermique model. *Remote Sensing of Environment* 198,
1065 160–172.
- 1066 Jacob, F., Oliosio, A., Gu, X.F., Su, Z., Seguin, B., 2002. Mapping surface
1067 fluxes using airborne visible, near infrared, thermal infrared remote sensing
1068 data and a spatialized surface energy balance model. *Agronomie* 22, 669–680.
- 1069 Jacob, F., Petitcolin, F., Schmugge, T., Vermote, E., French, A., Ogawa, K.,
1070 2004. Comparison of land surface emissivity and radiometric temperature
1071 derived from modis and aster sensors. *Remote Sensing of Environment* 90,
1072 137–152.
- 1073 Jacob, F., Schmugge, T., Oliosio, A., French, A., Courault, D., Ogawa, K.,
1074 Petitcolin, F., Chehbouni, G., Pinheiro, A., Privette, J., 2008. Modeling and
1075 inversion in thermal infrared remote sensing over vegetated land surfaces, in:
1076 *Advances in Land Remote Sensing*. Springer, pp. 245–291.

- 1077 Jacob, F., Vidal, T.H., Lesaignoux, A., Oliosio, A., Weiss, M., Nerry, F., Jacque-
1078 moud, S., Gamet, P., Caillault, K., Labarre, L., et al., 2021. A simulation-
1079 based error budget of the tes method for the design of the spectral configu-
1080 ration of the micro-bolometer-based mistigri thermal infrared sensor. *IEEE*
1081 *Transactions on Geoscience and Remote Sensing* .
- 1082 Jiménez-Muñoz, J., Sobrino, J., 2006. Error sources on the land surface tem-
1083 perature retrieved from thermal infrared single channel remote sensing data.
1084 *International Journal of Remote Sensing* 27, 999–1014.
- 1085 Jiménez-Muñoz, J.C., Sobrino, J.A., Mattar, C., Hulley, G., Göttsche, F.M.,
1086 2014. Temperature and emissivity separation from msg/seviri data. *IEEE*
1087 *Transactions on Geoscience and Remote Sensing* 52, 5937–5951.
- 1088 Koetz, B., Bastiaanssen, W., Berger, M., Defournay, P., Del Bello, U., Drusch,
1089 M., Drinkwater, M., Duca, R., Fernandez, V., Ghent, D., et al., 2018. High
1090 spatio-temporal resolution land surface temperature mission-a copernicus can-
1091 didate mission in support of agricultural monitoring, in: *IGARSS 2018-2018*
1092 *IEEE International Geoscience and Remote Sensing Symposium*, IEEE. pp.
1093 8160–8162.
- 1094 Lagouarde, J.P., Bach, M., Sobrino, J.A., Boulet, G., Briottet, X., Cherchali,
1095 S., Coudert, B., Dadou, I., Dedieu, G., Gamet, P., et al., 2013. The misti-
1096 gri thermal infrared project: scientific objectives and mission specifications.
1097 *International Journal of Remote Sensing* 34, 3437–3466.
- 1098 Lagouarde, J.P., Bhattacharya, B., Crébassol, P., Gamet, P., Adlakha, D.,
1099 Murthy, C., Singh, S., Mishra, M., Nigam, R., Raju, P., et al., 2019.
1100 Indo-french high-resolution thermal infrared space mission for earth natu-
1101 ral resources assessment and monitoring-concept and definition of trishna, in:
1102 *ISPRS-GEOGLAM-ISRS Joint International Workshop on “Earth Observa-*
1103 *tions for Agricultural Monitoring”*, p. 403.
- 1104 Lagouarde, J.P., Bhattacharya, B., Crébassol, P., Gamet, P., Babu, S., Boulet,
1105 G., Briottet, X., Buddhiraju, K.M., Cherchali, S., Dadou, I., et al., 2018. The

- 1106 indian-french trishna mission: Earth observation in the thermal infrared with
1107 high spatio-temporal resolution, in: IGARSS 2018-2018 IEEE International
1108 Geoscience and Remote Sensing Symposium, IEEE. pp. 4078–4081.
- 1109 Li, Z.L., Tang, B.H., Wu, H., Ren, H., Yan, G., Wan, Z., Trigo, I.F., Sobrino,
1110 J.A., 2013. Satellite-derived land surface temperature: Current status and
1111 perspectives. *Remote Sensing of Environment* 131, 14–37.
- 1112 Louchart, X., Voltz, M., 2007. Aging effects on the availability of herbicides to
1113 runoff transfer. *Environmental science & technology* 41, 1137–1144.
- 1114 Malenovský, Z., Rott, H., Cihlar, J., Schaepman, M.E., García-Santos, G., Fer-
1115 nandes, R., Berger, M., 2012. Sentinels for science: Potential of sentinel-1,-2,
1116 and-3 missions for scientific observations of ocean, cryosphere, and land. *Re-
1117 mote Sensing of Environment* 120, 91–101.
- 1118 Matsunaga, T., 1994. A temperature-emissivity separation method using an
1119 empirical relationship between the mean, the maximum, and the minimum
1120 of the thermal infrared emissivity spectrum. *Journal of the Remote Sensing
1121 Society of Japan* 14, 230–241.
- 1122 Mira, M., Olioso, A., Gallego-Elvira, B., Courault, D., Garrigues, S., Marloie,
1123 O., Hagolle, O., Guillevic, P., Boulet, G., 2016. Uncertainty assessment of
1124 surface net radiation derived from landsat images. *Remote sensing of Envi-
1125 ronment* 175, 251–270.
- 1126 Mira, M., Schmugge, T.J., Valor, E., Caselles, V., Coll, C., 2009. Comparison
1127 of thermal infrared emissivities retrieved with the two-lid box and the tes
1128 methods with laboratory spectra. *IEEE transactions on geoscience and remote
1129 sensing* 47, 1012–1021.
- 1130 Montes, C., Jacob, F., 2017. Comparing landsat-7 etm+ and aster imageries
1131 to estimate daily evapotranspiration within a mediterranean vineyard water-
1132 shed. *IEEE Geoscience and Remote Sensing Letters* 14, 459–463.

- 1133 Montes, C., Lhomme, J.P., Demarty, J., Prévot, L., Jacob, F., 2014. A three-
1134 source svat modeling of evaporation: Application to the seasonal dynamics of
1135 a grassed vineyard. *Agricultural and forest meteorology* 191, 64–80.
- 1136 Murphy, R.E., 2006. The npoess preparatory project, in: *Earth Science Satellite*
1137 *Remote Sensing*. Springer, pp. 182–198.
- 1138 Neinavaz, E., Skidmore, A.K., Darvishzadeh, R., 2020. Effects of prediction
1139 accuracy of the proportion of vegetation cover on land surface emissivity
1140 and temperature using the ndvi threshold method. *International Journal of*
1141 *Applied Earth Observation and Geoinformation* 85, 101984.
- 1142 Ogawa, K., Schmugge, T., Jacob, F., French, A., 2002. Estimation of broadband
1143 land surface emissivity from multi-spectral thermal infrared remote sensing.
1144 *Agronomie* 22, 695–696.
- 1145 Ogawa, K., Schmugge, T., Jacob, F., French, A., 2003. Estimation of land
1146 surface window (8–12 μm) emissivity from multi-spectral thermal infrared
1147 remote sensing—a case study in a part of sahara desert. *Geophysical Research*
1148 *Letters* 30.
- 1149 Olioso, A., 1995. Simulating the relationship between thermal emissivity and
1150 the normalized difference vegetation index. *International Journal of Remote*
1151 *Sensing* 16, 3211–3216.
- 1152 Olioso, A., Inoue, Y., Ortega-Farias, S., Demarty, J., Wigneron, J.P., Braud,
1153 I., Jacob, F., Lecharpentier, P., Ottlé, C., Calvet, J.C., et al., 2005. Future
1154 directions for advanced evapotranspiration modeling: Assimilation of remote
1155 sensing data into crop simulation models and svat models. *Irrigation and*
1156 *Drainage Systems* 19, 377–412.
- 1157 Olioso, A., Jacob, F., Weiss, M., 2018. First evaluation of land surface emissiv-
1158 ity spectra simulated with the sail-thermique model, in: *IGARSS 2018-2018*
1159 *IEEE International Geoscience and Remote Sensing Symposium, IEEE*. pp.
1160 3951–3954.

- 1161 Palluconi, F., Hoover, G., Alley, R., Jentoft-Nilsen, M., Thompson, T., 1999.
1162 An atmospheric correction method for aster thermal radiometry over land.
1163 Algorithm Theoretical Basis Document .
- 1164 Pardo, N., Sánchez, M.L., Timmermans, J., Su, Z., Pérez, I.A., García, M.A.,
1165 2014. Sebs validation in a spanish rotating crop. *Agricultural and Forest*
1166 *Meteorology* 195, 132–142.
- 1167 Poutier, L., Miesch, C., Lenot, X., Achard, V., Boucher, Y., 2002. Comanche
1168 and cochise: two reciprocal atmospheric codes for hyperspectral remote sens-
1169 ing, in: *2002 AVIRIS Earth Science and Applications Workshop Proceedings*,
1170 pp. 1059–0889.
- 1171 Realmuto, V., 1990. Separating the effects of temperature and emissivity: Emis-
1172 sivity spectrum normalization, in: *Proc. of the Second Thermal Infrared Mul-*
1173 *tispectral Scanner (TIMS) Workshop*, Jet Propulsion Lab., 1990, pp. 31–35.
- 1174 Ren, H., Liu, R., Yan, G., Li, Z.L., Qin, Q., Liu, Q., Nerry, F., 2015. Perfor-
1175 mance evaluation of four directional emissivity analytical models with thermal
1176 sail model and airborne images. *Optics express* 23, A346–A360.
- 1177 Richter, R., Coll, C., 2002. Bandpass-resampling effects for the retrieval of
1178 surface emissivity. *Applied Optics* 41, 3523–3529.
- 1179 Schmugge, T., French, A., Ritchie, J.C., Rango, A., Pelgrum, H., 2002. Tem-
1180 perature and emissivity separation from multispectral thermal infrared obser-
1181 vations. *Remote Sensing of Environment* 79, 189–198.
- 1182 Schmugge, T., Hook, S., Coll, C., 1998. Recovering surface temperature and
1183 emissivity from thermal infrared multispectral data. *Remote Sensing of En-*
1184 *vironment* 65, 121–131.
- 1185 Schmugge, T., Ogawa, K., Jacob, F., French, A., Hsu, A., Ritchie, J., Rango,
1186 A., 2003. Validation of emissivity estimates from aster data, in: *International*
1187 *Geoscience and Remote Sensing Symposium*, pp. III–1873.

- 1188 Schröder, W., Schmidt, G., Hasenclever, J., 2006. Geostatistical analysis of
1189 data on air temperature and plant phenology from baden-württemberg (ger-
1190 many) as a basis for regional scaled models of climate change. *Environmental*
1191 *Monitoring and Assessment* 120, 27–43.
- 1192 Seguin, B., Becker, F., Phulpin, T., Gu, X., Guyot, G., Kerr, Y., King, C.,
1193 Lagouarde, J., Ottlé, C., Stoll, M., Tabbagh, A., Vidal, A., 1999. Irsute: a
1194 minisatellite project for land surface heat flux estimation from field to regional
1195 scale. *Remote Sensing of Environment* 68, 357–369.
- 1196 Sobrino, J., Caselles, V., 1990. Thermal infrared radiance model for interpret-
1197 ing the directional radiometric temperature of a vegetative surface. *Remote*
1198 *Sensing of Environment* 33, 193–199.
- 1199 Sobrino, J., Lagouarde, J., Boulet, G., Briottet, X., Cherchali, S., Coudert, B.,
1200 Dadou, I., Dedieu, G., Gillespie, A., Hagolle, O., et al., 2010. Overview of the
1201 thermal infrared explorer (tirex) mission. *Proc. Abstract Book 3rd Recent*
1202 *Adv. Quantitative Remote Sens* , 213–214.
- 1203 Sobrino, J.A., Del Frate, F., Drusch, M., Jiménez-Muñoz, J.C., Manunta, P.,
1204 Regan, A., 2016. Review of thermal infrared applications and requirements for
1205 future high-resolution sensors. *IEEE Transactions on Geoscience and Remote*
1206 *Sensing* 54, 2963–2972.
- 1207 Sobrino, J.A., Jiménez-Muñoz, J.C., 2014. Minimum configuration of thermal
1208 infrared bands for land surface temperature and emissivity estimation in the
1209 context of potential future missions. *Remote Sensing of Environment* 148,
1210 158–167.
- 1211 Sobrino, J.A., Jimenez-Munoz, J.C., Paolini, L., 2004. Land surface temperature
1212 retrieval from landsat tm 5. *Remote Sensing of environment* 90, 434–440.
- 1213 Sobrino, J.A., Jiménez-Muñoz, J.C., Verhoef, W., 2005. Canopy directional
1214 emissivity: Comparison between models. *Remote Sensing of Environment* 99,
1215 304–314.

- 1216 Tonooka, H., 2005. Accurate atmospheric correction of aster thermal infrared
1217 imagery using the wvs method. *IEEE Transactions on Geoscience and Remote*
1218 *Sensing* 43, 2778–2792.
- 1219 Vanhellemont, Q., 2020. Combined land surface emissivity and temperature
1220 estimation from landsat 8 oli and tirs. *ISPRS Journal of Photogrammetry*
1221 *and Remote Sensing* 166, 390–402.
- 1222 Vidal, T.H., Jacob, F., Olioso, A., Gamet, P., 2021. Optimization of instrumen-
1223 tal spectral configurations for the split-window method in the context of the
1224 trishna mission. *IEEE Transactions on Geoscience and Remote Sensing* .
- 1225 Vinukollu, R.K., Wood, E.F., Ferguson, C.R., Fisher, J.B., 2011. Global es-
1226 timates of evapotranspiration for climate studies using multi-sensor remote
1227 sensing data: Evaluation of three process-based approaches. *Remote Sensing*
1228 *of Environment* 115, 801–823.
- 1229 Weiss, M., Jacob, F., Duveiller, G., 2020. Remote sensing for agricultural ap-
1230 plications: A meta-review. *Remote Sensing of Environment* 236, 111402.
- 1231 Yan, G., Jiao, Z.H., Wang, T., Mu, X., 2020. Modeling surface longwave radia-
1232 tion over high-relief terrain. *Remote Sensing of Environment* 237, 111556.
- 1233 Zheng, X., Li, Z.L., Nerry, F., Zhang, X., 2019. A new thermal infrared channel
1234 configuration for accurate land surface temperature retrieval from satellite
1235 data. *Remote Sensing of Environment* 231, 111216.